Master's thesis

NTNU
Norwegian University of Science and Technology
Faculty of Natural Sciences
Department of Physics

Tarje Arntzen Røger

On the effects of a non-infinitesimal nuclear charge distribution on the hyperfine spectrum of Bi I

Master's thesis in physics
Supervisor: Jonas Rolf Persson
May 2024

NTNU
Norwegian University of
Science and Technology

Tarje Arntzen Røger

On the effects of a non-infinitesimal nuclear charge distribution on the hyperfine spectrum of Bi I

Master's thesis in physics
Supervisor: Jonas Rolf Persson
May 2024

Norwegian University of Science and Technology
Faculty of Natural Sciences
Department of Physics

NTNU
Norwegian University of
Science and Technology

Abstract

The Breit-Rosenthal effect for the five $6p^3$ ground states of bismuth, $^2P^o_{1/2}$, $^4S^o_{3/2}$, $^2D^o_{3/2}$, $^2P^o_{3/2}$, and $^2D^o_{5/2}$, were examined using a multiconfigurational Dirac-Hartree-Fock approach with relativistic and quantum electrodynamical corrections included in a configuration interaction calculation (MCDHF-CI), using the general-purpose relativistic atomic structure package GRASP2018. Concurrently, an exploration of the optimal expansions in the active set approach was done. Based on the calculations, with the Breit-Rosenthal effect quantified as $\Delta_{BR} = \lambda\delta\langle r^2\rangle$, the following recommendations for the proportionality constant λ were found: $\lambda(^2P^o_{1/2}) = -0.039(2)$ %fm^{-2}, $\lambda(^4S^o_{3/2}) = -0.249(10)$ %fm^{-2}, $\lambda(^2D^o_{3/2}) \approx -0.1$ %fm^{-2}, $\lambda(^2P^o_{3/2}) = 0.105(26)$ %fm^{-2}, and $\lambda(^2D^o_{5/2}) = -0.017(8)$ %fm^{-2}. An attempt was made at comparing the calculated Breit-Rosenthal effect with the hyperfine anomalies between ^{209}Bi and 12 other bismuth isotopes, though the uncertainties in the available experimental data made such comparison difficult. The exploration of the active set approach showed that rather than achieving better accuracy by indiscriminately expanding the active space, better results at far lower computational cost can be achieved by systematic and strategic expansion of it. Better convergence towards experimentally measured values were achieved for expansions consisting of $\approx$ 30 000 configurations, than for expansions in excess of 700 000 configurations.

Sammendrag

Størrelsen på Breit-Rosenthal-effekten ble estimert for de fem $6p^3$-grunntilstandene i vismut, $^2P^o_{1/2}$, $^4S^o_{3/2}$, $^2P^o_{3/2}$, $^2D^o_{3/2}$, og $^2D^o_{5/2}$. Utregningene ble gjort med en multikonfigurasjons Dirac-Hartree-Fock-metode, med konfigurasjonsinteraksjons-utregninger gjort for å korrigere for relativistiske og kvanteelektrodynamiske effekter (MCDHF-CI). Samtidig ble det gjort en vurdering av den optimale mengden konfigurasjoner som inkluderes i beregningene, mot oppnådd presisjon, med aktivt-sett-metoden. Basert på utregningene, med Breit-Rosenthal-effekten kvantifisert som $\Delta_{BR} = \lambda\delta\langle r^2\rangle$, vil de følgende verdiene kunne anbefales for proporsjonalitetskonstanten λ: $\lambda(^2P^o_{1/2}) = -0.039(2)$ %fm^{-2}, $\lambda(^4S^o_{3/2}) = -0.249(10)$ %fm^{-2}, $\lambda(^2D^o_{3/2}) \approx -0.1$ %fm^{-2}, $\lambda(^2P^o_{3/2}) = 0.105(26)$ %fm^{-2}, og $\lambda(^2D^o_{5/2}) = -0.017(8)$ %fm^{-2}. Resultatene samsvarer i størrelsesorden med tilsvarende undersøkelser gjort på kvikksølv og bly. Et forsøk ble gjort på å estimere hvor stor andel av hyperfinanomaliene mellom ulike vismut-isotoper Breit-Rosenthal-effekten utgjør, men grunnet stor usikkerhet i tilgjengelige eksperimentelle data, var det ikke mulig å treffe en sikker konklusjon. Hva angår aktivt-sett-metoden, ble det funnet at en strategisk og systematisk utvidelse av det aktive settet gav høyere presisjon med mindre bruk av dataressurser enn mindre "forsiktige" utvidelser.

Unit system

Hartree atomic units will be used throughout this thesis, unless otherwise specified. In this system, the following quantities are all set to unity:

- Electron mass, m_e
- Elementary charge, e
- The inverse Coulomb constant, $4\pi\epsilon_0$
- The reduced Planck constant, $\hbar = h/2\pi$

Of note is the fact that in this system, the speed of light is written as the inverse of the fine-structure constant: $c = \alpha^{-1}$.

Contents

List of Figures

List of Tables

List of abbreviations

ASF	Atomic state function
bash	Bourne-again shell
CAS	Complete active space
CSF	Configuration state function
D	Double
GRASP	General-purpose relativistic atomic structure package
GRASP2018	General-purpose relativistic atomic structure package 2018
hpc	High-performance computing
MPI	Message passing interface
MR	Multireference
NTNU	Norwegian University of Science and Technology
QED	Quantum electrodynamics/quantum electrodynamical
RAS	Restricted active space
S	Single
SD	Single-double
SDT	Single-double-triple
SrD	Single-restricted-double
T	Triple

Chapter 1

Introduction

In measuring atomic or nuclear parameters, such as the electromagnetic multipole moments, the experimental methods available at the present time may not be generally applicable. One may for instance run into trouble when dealing with radioactive isotopes that decay before a measurement can be done, or in producing and storing high-quality, clean samples of the isotopes. In the present work, one way of bypassing these issues will be presented; given a stable reference isotope[1], one can infer the properties of other isotopes by establishing relations between measurable quantities and variations in certain key parameters. One such inference can be made for the values of the magnetic dipole moment μ, which can be calculated for some isotope using values acquired for some reference isotope, with [1]

$$\mu' = \mu_{ref} \frac{I'}{I_{ref}} \frac{A'}{A_{ref}} \tag{1.1}$$

A here denoting the magnetic dipole hyperfine constants, and I the nuclear spins of the isotopes. This approximation is based on a model of the nucleus as a perfect magnetic dipole. In reality, the nucleus is an extended charge- and current distribution, giving rise to the Breit-Rosenthal and Bohr-Weisskopf effects, respectively, which have to be accounted for. By quantifying these effects, the uncertainties on values of magnetic dipole moments may be reduced along chains of isotopes, based on the calculations done on a reference isotope. In the following thesis, a parametric study of the Breit-Rosenthal effect in the neutral Bi I isotopes using a multiconfiguration Dirac-Hartree-Fock method with a configuration interaction calculation (MCDHF-CI) will be reported. The size of the effect will be determined by considering the dependence of the dipole magnetic hyperfine constant A on variations in two parameters, the nuclear mean squared charge radius, and the nuclear skin thickness, in the reference isotope ^{209}Bi.

[1] Now, the isotope considered in this work is not actually stable. ^{209}Bi decays by α-particle emission, though with a half-life of $2 \cdot 10^{19}$ years, it can be treated as stable. It is also the only naturally occurring bismuth isotope, making it the obvious choice for a reference isotope in the present work.

Calculations were done using the general-purpose relativistic atomic structure package (GRASP2018, henceforth denoted by just "GRASP").

1.1 Thesis structure

The thesis will start off, in chapter 2, with a brief historical perspective on the interconnection between atomic structure and -spectroscopy, ending with a qualitative discussion of the modern atomic model. Chapters 3 through 6 will set up the theory underlying the calculations, following along with the workflow of a single calculation of the hyperfine constant (see figure 1.1). In order, the topics covered here will be the nuclear and electronic models used in GRASP, the self-consistent calculation of the wave functions using multiconfigurational Dirac-Hartree-Fock theory, the application of relativistic and quantum electrodynamical (QED) effects in the configuration interaction calculation, before a discussion of hyperfine structure rounds out the theory section. After that, the methods of the present work will be discussed in chapters 7 and 8, with special focus on the exploration of optimal expansions with regards to the balancing of computational resource use and accuracy. Finally, the results of the calculations will be reported in chapter 9, and discussed in chapter 10, before the whole thesis is concluded in chapter 11. In addition to the structure outlined above, three appendices are included, containing examples of the scripting of calculations, a figure to be discussed in chapter 9, and complete expansion sizes for the methods to be discussed.

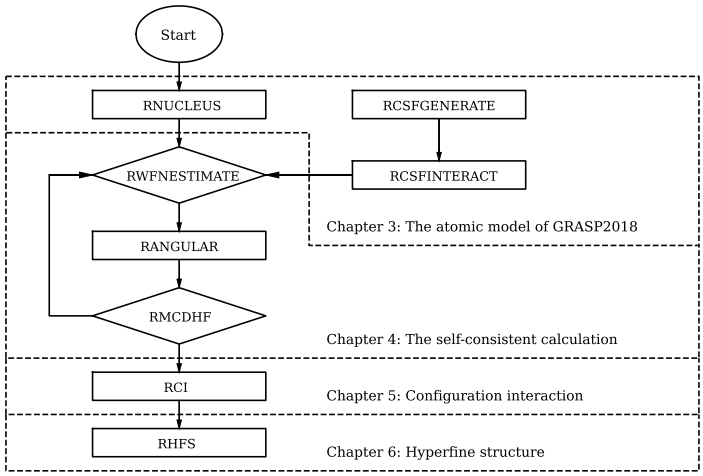

Figure 1.1: Flowchart outlining both a single calculation of the hyperfine constant, as well as the structure of the theory section of the thesis. The arrow going from RMCDHF to RWFNESTIMATE indicates that previously calculated wave functions may be used as input for subsequent calculations, improving accuracy and reducing computational cost.

1.2 Motivation

The *raison d'être* of this thesis, is to provide calculations which in turn can be used to decrease uncertainties in the measured values of the magnetic dipole moment of bismuth [2]. In addition, the methodology which is typically applied to similar atomic structure calculations will be examined, hopefully providing results applicable to further research within the field. The study of atomic structure generally, and hyperfine structure specifically has applications in everything from classifying astronomical objects, to leading up to tests of some of the most accurate theories currently known, like QED. In addition to these concrete benefits, and as will be discussed later in this thesis, there is an inherent value in comparing theory to experiment, as thus far unnoticed discrepancies may be found, further deepening our understanding of the fundamental laws that govern our existence.

1.3 Theoretical background

As a last note before getting into the actual thesis: it is assumed that the reader is familiar with the physics and terminology of atomic systems. For those to whom that does not apply, some standard texts within this topic are "The Theory of Atomic Structure and Spectra" by R. D. Cowan [3], as well as "The Theory of Atomic Spectra" by E. U. Condon and G. H. Shortley [4].

Chapter 2

A brief look at the development of atomic physics

In the same manner as for archaeological finds, removing a physical phenomenon from its proper context may render it meaningless to the observer. Therefore, this chapter will give a brief account of the development of the modern atomic model.

2.1 History of atomic physics

As detailed in the book "Inward Bound" by Abraham Pais [5], the study of atomic spectra were of major importance to the development of not only the models used to describe the atom, but of quantum mechanics as a whole. The spark that ignited the "quantum revolution"[1] was Planck's *ad hoc* assumption on the quantum nature of light emission in describing blackbody radiation [5]. In the years around the turn of the century, a time in which great leaps in our understanding of matter occurred, atomic spectra and the physical structure of atoms were developed in tandem. During this time, there were a few curious atomic models in circulation, from Thomson's description of the atom as alike an English plum pudding, to Nagaoka's speculation that the atom was like Saturn, with electrons orbiting a central body like the gas giant's rings, to the entire line of thought that atoms were built up from hundreds or thousands of electrons, no massive positive charge in sight [5]. Though some were more prescient than others, these interpretations and thought experiments have been left by the wayside of history. It was, however, in this time of intense speculation, that

[1] Pais raises the excellent question "as seen by whom?" with regards to terms like "scientific revolution", due to the importance of Planck's quantum hypothesis going somewhat unnoticed for a time after it was posed.

Bohr proposed his atomic model, combining the quantum hypothesis of Planck, with the atomic structure theorized by Rutherford[2]: a positive nucleus with electrons moving in circular orbits around it, akin to a planet orbited by moons, except that the electrons could only assume specific orbits corresponding to the energy state of the atom. Bohr's atomic model can even today be used as a pedagogical tool, as it does not deviate too far from the general structure of the atom, in addition to it describing the properties of atomic spectra in an intuitive way.

One of the great successes of Bohr's model, was that its predicted spectral lines for hydrogen coincided with the Balmer series, the empirically found formula describing some of the spectral lines of that element:

$$k = R_H\left(\frac{1}{2^2} - \frac{1}{n^2}\right), n > 2 \tag{2.1}$$

k here being the wavenumber of the photon making up a line in the hydrogen spectrum, and R_H being the Rydberg constant for hydrogen.

In Bohr's theory, the wavenumber of the photon emitted in a transition between two states i and f, is given by [6, p. 103]

$$k = R_\infty\left(\frac{1}{n_f^2} - \frac{1}{n_i^2}\right), n_i > n_f \tag{2.2}$$

With the n's now known to represent specific energy states of the atom, and R_∞ being given by (in SI units)

$$R_\infty = \left(\frac{1}{4\pi\epsilon_0}\right)^2 \frac{me^4}{4\pi\hbar^3 c} \tag{2.3}$$

which by experimental verification is very nearly equal to R_H [6, p. 103]. If $n_f = 2$ is inserted into equation (2.2), the Balmers series is reproduced.

This example illustrates that the correct description of atomic spectra was a priority in the development of the modern atomic model, and that even as far back as the beginning of the previous century, atomic theory was already quite sophisticated. However, the Bohr model is not the end of the line[3]. As the Schrödinger equation laid the groundwork for the more complete theory of quantum mechanics, our understanding of the atom continued to develop.

[2]Based on the scattering angles measured by firing α particles at a thin gold foil, an experiment carried out by Marsden and Geiger, Rutherford came up with a description of the atom as mostly empty, with a central charge heavy enough for high-energy α-particles to scatter off.

[3]Already in Bohr's time, refinements to the model were made, for instance by introducing elliptical orbits, known as Bohr-Sommerfeld orbits. The jump is made directly from the Bohr model to the modern one, as only the broad strokes of this history is necessary to set the context for this thesis.

2.2 Modern atomic theory

The modern atomic model is somewhat less intuitive than that of Bohr. Instead of ball-like electrons in circular orbits around a hard nucleus, the electrons must be described as a cloud of probability surrounding a "fuzzy" nucleus with no clear edge. In this model, the wave functions of the electrons may even be non-vanishing at the atomic centre, giving a non-zero percent chance of finding an electron within the nucleus, a fact that is of great importance to the effect studied in this thesis.

The equations describing the energy states of the modern atom are solutions to either the Schrödinger equation, in the non-relativistic case, or the Dirac equation, in the relativistic one. The non-relativistic approximation is mainly valid for light atoms, whereas heavier atoms require a relativistic treatment, either in full, using the Dirac equation, or as corrective terms to the non-relativistic Hamiltonian, using the Breit-Pauli approximation. Due to the complexity[4] of atomic systems, exact solutions are only possible for a very few number of atoms, mainly hydrogen, and hydrogen-like systems [7, p. 6]. Since the object of study for this thesis, ^{209}Bi, is both heavy and complex, solutions of its equations of motion require relativistic approximations, which will be discussed in later chapters.

2.2.1 On the electron cloud

In the modern understanding of atomic theory, the electrons surround the nucleus as a cloud of probability; wave functions which only have determinate positions when measured. These wave functions can be quite complex and beautiful, as showcased in figure 2.1.

[4] By "complexity" is meant that the atom contains many electrons, requiring the use of atomic many-body theory.

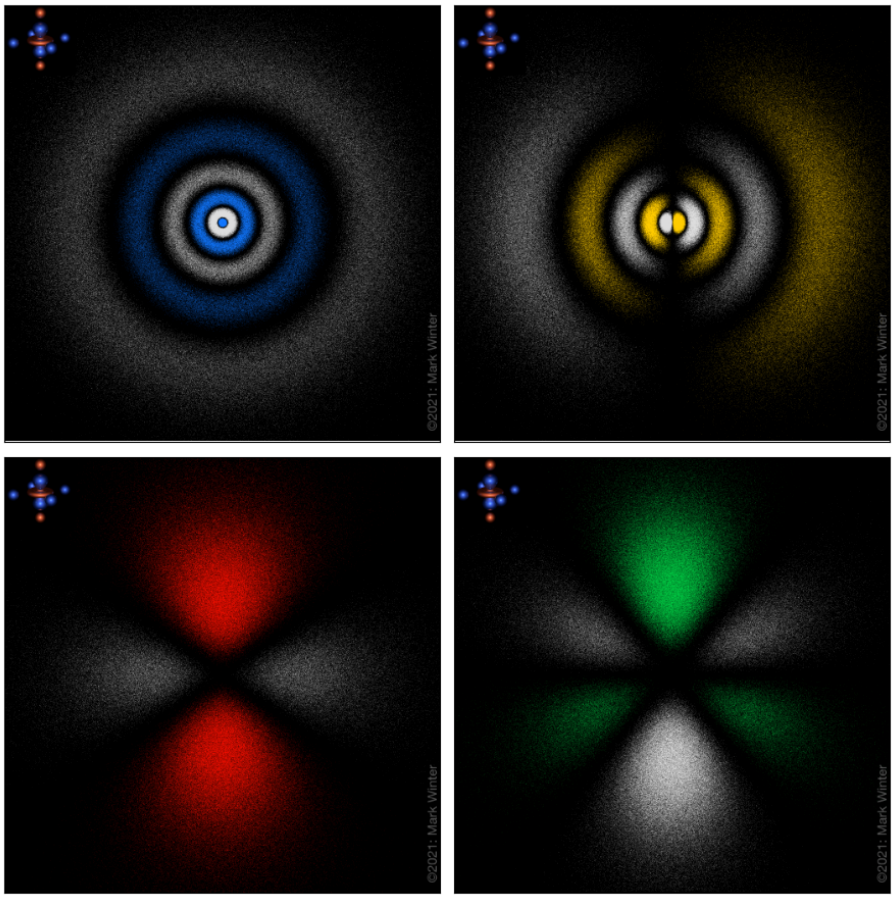

Figure 2.1: Electron orbitals belonging to 6s (blue), 6p (yellow), 3d (red), and 4f (green). Higher density of dots indicate a higher probability of finding an electron in an area.
Image source: https://winter.group.shef.ac.uk/orbitron/

As can be seen in the figure above, the probability distribution of the s orbital does not, in fact, vanish towards the nuclear centre. This is also true for the relativistic $p_{1/2}$ orbitals (more on relativistic orbitals later). Since the goal of the current study is to quantify the effect of variations in the spatial distribution of the nucleus on the hyperfine structure of the atom, such orbitals are of special significance.

Though the Bohr model has been supplanted, it's explanation of atomic spectra still holds, to a large degree. When an atom is excited, for instance by heat or specifically tuned lasers, the added energy may cause an electron to move from its ground state orbital, to one of a higher energy. With a bit of careful anthropomorphizing, we can say that the atom now "wants" to return to

its ground state of lower energy, and as such needs to get rid of the energy added by the excitation. It achieves this by emitting photons, the total energy of which must exactly match the energy added to the system in the first place. These photons are emitted when an electron moves from a higher to a lower orbital, and thus the atom can only emit photons of frequencies matching specific, discrete energy differences. By exciting atoms, and measuring the energies of the photons emitted by their relaxation, one acquires a spectrum made up of all the different allowed transition energies, characteristic for each atomic species.

Electronic shell model

The reason for the discreteness of atomic energy states is the Pauli exclusion principle, which states that two fermions, the class of particle to which the electron belongs, may not simultaneously exist in the exact same state. An electron in the cloud of an atom has a quantum state that can be described in terms of four[5] quantum numbers, those being the principal quantum number n, which describes electron's energy level, the azimuthal quantum number l, describing the orbital of the electron, and the magnetic quantum numbers m_l and m_s, which describe the orientation of the orbital and the spin state of the electron, respectively.

The principal quantum number can take any integer value ≥ 1:

$$n = 1, 2, 3, 4, ...$$

The azimuthal quantum number can take any value from zero to $n - 1$, and is, for historical reasons, denoted by letters in the fashion shown in the table below.

Table 2.1: The first 8 azimuthal quantum numbers, and their corresponding letter symbol. After k, the rest are in alphabetical order, only omitting s and p due to them being represented by $l = 0, 1$.

l =	0	1	2	3	4	5	6	7
Denoted by:	s	p	d	f	g	h	i	k

The orbital magnetic quantum number may take any value $m_l \in [-l, l]$, and the spin quantum numbers can only take on two values, those being $m_s = \pm 1/2$, representing electrons of the spin-up and spin-down varieties, respectively.

Each shell may contain up to n subshells, where each subshell may contain up to $2(l + 1)$ orbitals, within each of which a maximum of two electrons may reside. The filling of a subshell is usually denoted on the form $(nl)^w$, where w is the number of electrons in said subshell. For atomic systems consisting of m subshells, the notation becomes

[5] As will be discussed shortly, this is not the case in the relativistic regime.

$$(n_1 l_1)^{w_1}(n_2 l_2)^{w_2}(n_3 l_3)^{w_3}...(n_m l_m)^{w_m} \tag{2.4}$$

Now, in systems which must be treated relativistically, the subshells are denoted with an additional quantum number j, which is an eigenvalue to the total angular momentum operator $\boldsymbol{J} = \boldsymbol{L} + \boldsymbol{S}$, seeing as l and s are no longer good[6] quantum numbers on their own. A relativistic subshell is thus defined not by nl, but by nlj.

For larger systems, a useful shorthand is to find the largest noble gas whose electronic structure one can build from the filled subshells in an atom, and gather those subshells into a symbol representing said gas. For instance, the electronic structure of neutral bismuth in the ground state may be represented by the following

$$[\mathrm{Xe}] + 4f^{14}5d^{10}6s^2 6p^3$$

Due to Xenon having filled $n = 1, 2, 3$ shells, along with the subshells 4s4p4d5s5p.

2.2.2 On the nucleus

Far from being the ball of positive charge often found in simplistic illustrations of the atom, the nucleus is a complicated entity, with a rich inner life. The nucleus is built up of two types of particles, called nucleons: the proton with charge $+e$, and the neutron with no charge. Each of these is in turn made up of two types of particle found in the Standard Model of particle physics, quarks and gluons. This inner structure of the nucleons requires quantum chromodynamics (QCD) to explain, and is outside the scope of this thesis. A discussion on the nuclear model employed by GRASP will be given in chapter 3.

Nuclear shell model

Akin to the electron cloud, the nucleus is also filled in a structured fashion. Protons and neutrons have separate shells, that are filled independently of one another. Both are filled at the same number of their respective nucleons, which are 2, 8, 20, 28, 40, 50, 82, and 126 [8, p. 245]. These are called the *magic numbers* of the nuclear shell model, and isotopes with magic numbers of either protons or neutrons tend to be more stable than their non-magic counterparts, due to such nuclei having higher binding energies. The object of study for this thesis, ^{209}Bi, has 83 protons and 126 neutrons, only a single proton away from being *doubly magic*.

Also analogously to the electron shells, the nucleons within a shell create spin-up spin-down pairs, resulting in a contribution of zero to the total nuclear spin. Thus, the spin properties of the nucleus is dependent on the unpaired nucleons. In the case of ^{209}Bi, we have a closed neutron shell ($N = 126$), and

[6] A good quantum number is one corresponding to a conserved quantity.

a single unpaired proton ($Z = 83$), being a $h_{9/2}$ proton, giving a total nuclear spin of $I = 9/2$.

Chapter 3

The atomic model of GRASP2018

According to the flowchart seen in figure 1.1, the first steps in a calculation of the magnetic dipole hyperfine constant are to define the properties of the isotope, in terms of the nuclear structure of the atom, and the manner in which electronic orbitals are included.

3.1 Defining the nucleus

The first step in the flowchart uses the program RNUCLEUS for defining the isotope in question, ^{209}Bi, in the present case. When running the program, the user is prompted to input eight parameters defining the charge, mass, spatial distribution, and angular momentum properties of the nucleus. These parameters, with the values used in the current project, are listed in table 3.1.

Table 3.1: Parameters used in defining the isotope ^{209}Bi. Note that the values of mean squared charge radius and skin thickness will be varied in later calculations. The parameters were found using the International Atomic Energy Agency's (IAEA) Livechart (accessed 12.05.2024). The sources are those listed in the Livechart.

Name	Symbol	Value
Atomic number	Z	83
Mass number	A	209
Mean squared charge radius[9]	$\langle r^2 \rangle^{1/2}$	5.5211(26) fm
Skin thickness	t	2.3 fm
Mass of neutral atom[10]	M	208.9803986(15) amu
Nuclear spin quantum number	I	9/2
Nuclear magnetic dipole moment[11]	μ_I	4.092(2) μ_N
Nuclear electric quadrupole moment[12]	Q	-0.516(15) b

In the table above, μ_N refers to the nuclear magneton, and is in SI units given by $\mu_N = e\hbar/2m_p$, m_p being the mass of the proton. The mean squared charge radius and skin thickness are used to define the two parameters of the Fermi distribution (see below). The latter two values, the multipole moments, are defined in terms of the expectation value of the nuclear multipole moment operator in the state in which the nuclear orbital magnetic quantum number has its maximal value, $M_I = I$[1]:

$$\mu_I = \langle \nu II | \mathbf{M}^{(1)} | \nu II \rangle \tag{3.1}$$

$$Q = 2\langle \nu II | \mathbf{M}^{(2)} | \nu II \rangle \tag{3.2}$$

As we will see later, in chapter 6, these values directly relate to the tensor algebra formulation of the magnetic dipole and electric quadrupole hyperfine constants, A and B, allowing for the calculation of the latter quantities knowing the former, or vice versa.

3.1.1 Nuclear model - The Fermi distribution

As hinted at in the historical perspective, the nucleus cannot be conceptualized as a hard ball of positive charge. A more accurate description would be to call it a charge- and current distribution that tapers off away from the nuclear centre,

[1]Note that for the remainder of this thesis, to follow the conventions of the field of theoretical atomic structure, the angular momentum quantum numbers will be denoted by capital letters.

rather than end abruptly. In the GRASP suite, this charge distribution[2] will be approximated using a two-parameter Fermi distribution, which can be shown to be valid for nuclei with mass numbers $A > 20$ [13, p. 28]:

$$\rho(r) = \frac{\rho_0}{1 + e^{(r-c)/a}} \tag{3.3}$$

Here, ρ_0 represents the nucleon density at the nuclear centre, c, is the distance at which the charge density is half of what it is at the nuclear centre, and a is related to the so-called skin thickness t, by $t = 4a \ln 3$; by simple manipulation of the expression above, it is easily seen that the skin thickness is the distance over which the charge density goes from 90% to 10% of its central value.

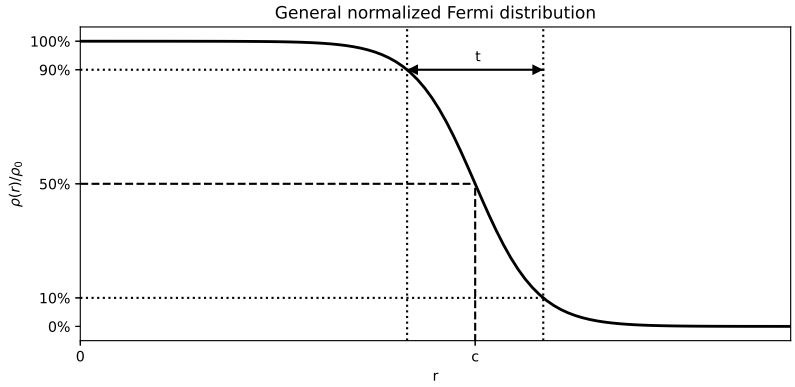

Figure 3.1: A general, normalized Fermi distribution, with c and t marked.

When choosing the nuclear parameters seen in table 3.1, the default values found in the RNUCLEUS program were opted for. The mean squared charge radius is safely anchored in the literature, being the value tabulated by Angeli and Marinova [9]. The skin thickness, however, is a bit less clear cut. In his monograph "Nuclear Sizes", Elton reports nuclear parameters for a selection of isotopes, including ^{209}Bi, found by electron scattering experiments. In that work, the skin thickness is reported as 2.7 fm, with error bars placing the value at least above 2.5 fm [13, pp. 31-32]. In 1987, De Vries, De Jager, and De Vries published a compilation of nuclear parameters, wherein the skin thickness of ^{209}Bi is reported as approximately 2.06 fm [14]. In the present project, the default value implemented in the RNUCLEUS program, $t = 2.3$ fm was used, as is in line with what is given in the "Handbook of Relativistic Quantum

[2]The properties arising from the extended current distribution (i.e. magnetization) of the nucleus will be mentioned in brief when dealing with hyperfine structure, in chapter 6, but is not the focus of this thesis. GRASP, at date of writing and to the author's knowledge, has no simple way of implementing the current distribution into the nuclear model used in the calculations.

Chemistry[3]" [15, p. 57]. Due to the small dependency of A on variations in skin thickness (see chapter 8), further pursuit of this topic was dropped.

3.2 Electron orbitals

It is a well known fact that many-body systems with mutual interactions between all N components, are not generally analytically solvable when $N > 2$. In atomic physics, this means that neither the Schrödinger equation nor the Dirac equation have general exact solutions for any atomic system other than those of the simple hydrogen-like class of atoms and ions. For this reason, the field of atomic many-body theory has to rely on approximations and simplifying models, for which solutions can be found. For an electronic orbital in an atomic system, two strict symmetries have to be obeyed:

1. The wave function must be anti-symmetric with respect to the interchange of any two electrons.
2. The Pauli exclusion principle must be respected, meaning that a wave function in which any two electrons share the same set of quantum numbers can not exist.

We will now develop the orbital wave functions used by the GRASP suite, in which these symmetries are shown to hold.

3.2.1 The relativistic central-field approximation

In the strictest sense, the potential felt by a single electron in the atomic cloud consists of the Coulomb attraction from the nucleus, as well as the Coulomb repulsion from all other electrons

$$V_i(r_i) = -\frac{Z}{r_i} + \sum_{\substack{j=1 \\ j \neq i}} \frac{1}{r_{ij}} \tag{3.4}$$

Where $r_{ji} = |\vec{r_j} - \vec{r_i}|$. Using this, we quickly encounter the difficulties of a many-body problem, as discussed above. If we rather assume that the potential from the other electrons can be written as a spherically symmetric, averaged potential measured relative to the atomic centre,

$$V_i(r_i) \approx V_{av}(r_i) \tag{3.5}$$

we can greatly simplify the calculations, as in doing so, the problem is reduced from a non-central many-body problem, to a central two-body problem, reducing the complexity of finding a solution. As will be discussed in chapter 4, this central-field assumption also forms the framework of the Hartree-Fock

[3]For the sake of transparency: the value was not selected based on the handbook, but on the default value in GRASP.

theory used to iteratively calculate the wave functions in the self-consistent calculation. With the central-field approximation in place, the Hamiltonian of a single electron becomes

$$\mathcal{H}_{CF} = \sum_i \left(\alpha_f^{-1} \vec{\alpha}_i \cdot \vec{p}_i + \alpha_f^{-2} (\beta_i - I_{4\times 4}) + V_{av}(r_i) \right) \tag{3.6}$$

With the kinetic energy operator in the expression above derived from the Dirac equation. Note that the fine-structure constant $\alpha \approx 1/137$ is here written with the subscript "f", to distinguish it from the α-matrices. These, and the β-matrix are given by

$$\vec{\alpha}_i = \begin{bmatrix} 0 & \vec{\sigma_i} \\ \vec{\sigma_i} & 0 \end{bmatrix}, \; \beta_i = \begin{bmatrix} I_{2\times 2} & 0 \\ 0 & -I_{2\times 2} \end{bmatrix} \tag{3.7}$$

with $\vec{\sigma}$ being the Pauli spin matrices, and $I_{n\times n}$ denoting the $n \times n$ identity matrix.

Since the Hamiltonian (3.6) only contains single-particle operators, we can write its eigenfunctions as products of many single-particle, or in this case, single-electron wave functions

$$\mathcal{H}_{CF} \Psi(\alpha; \boldsymbol{R}) = E_{CF} \Psi(\alpha; \boldsymbol{R}) \Rightarrow \Psi(\alpha; \boldsymbol{R}) = \prod_{i=1}^{N} \phi(\gamma_i; \vec{r}_i) \tag{3.8}$$

Where α are the quantum numbers defining the eigenfunction of the total central-field Hamiltonian, $\boldsymbol{R} = \{\vec{r}_1, \vec{r}_2, \ldots \vec{r}_m\}$ denotes the set of electron coordinates, and γ_i are the quantum numbers defining a state on the form [16, p. 99]

$$\phi(\gamma, \vec{r}) = \begin{pmatrix} \xi(\gamma; \vec{r}) \\ \bar{\xi}(\gamma; \vec{r}) \end{pmatrix} = \begin{pmatrix} r^{-1} P_{n\kappa}(r) \zeta_{\kappa m}(\theta, \varphi, \sigma) \\ i r^{-1} Q_{n\kappa}(r) \zeta_{-\kappa m}(\theta, \varphi, \sigma) \end{pmatrix} \tag{3.9}$$

Where P and Q are the so-called large and small radial components of the wave function, so-called as $Q \to 0$ in the non-relativistic regime. The function $\zeta_{\kappa m}(\theta, \varphi, \sigma)$ is defined by

$$\zeta_{\kappa m}(\theta, \varphi, \sigma) = \sum_{\nu, \mu} \langle s\nu l\mu | jm \rangle \chi_\nu(\sigma) Y_{l\mu}(\theta, \varphi) \tag{3.10}$$

$\chi_\nu(\sigma)$ being the spin eigenfunction of the system, $Y_{l\mu}(\theta, \varphi)$ representing the well known spherical harmonics, and $\langle s\nu l\mu | jm \rangle$ being the vector-coupling coefficients, also known as the Clebsch-Gordan coefficients. There is also a new quantum number at play here, κ, which is defined in terms of the spin- and orbital angular momentum operators, and the ζ-function defined above:

$$(\vec{\sigma} \cdot \vec{l} + 1) \zeta_{\kappa m} = -\kappa \zeta_{\kappa m} \tag{3.11}$$

and has the values

$$\kappa = l(l+1) - j(j+1) - \frac{1}{4} = \begin{cases} -(j+1/2) = -(l+1) & \text{for } j = l + 1/2 \\ (j+1/2) = l & \text{for } j = l - 1/2 \end{cases} \quad (3.12)$$

By using the fact that $\mathcal{H}_{CF}$ is invariant under permutations of the electron coordinates of (3.8), the product function may be used to form a wave function on the form of a Slater determinant [17, p. 9]

$$\Phi(\Gamma; \boldsymbol{R}) = \frac{1}{\sqrt{N!}} \begin{vmatrix} \phi(\gamma_1; \vec{r}_1) & \phi(\gamma_1; \vec{r}_2) & \dots & \phi(\gamma_1; \vec{r}_N) \\ \phi(\gamma_2; \vec{r}_1) & \phi(\gamma_2; \vec{r}_2) & \dots & \phi(\gamma_2; \vec{r}_N) \\ \vdots & \vdots & \ddots & \vdots \\ \phi(\gamma_N; \vec{r}_1) & \phi(\gamma_N; \vec{r}_2) & \dots & \phi(\gamma_N; \vec{r}_N) \end{vmatrix} \quad (3.13)$$

Here, Γ represents all quantum numbers defining the state. Now, from the basic properties of determinants, it is obvious that the exchange of any two sets of quantum numbers $\gamma_i \leftrightarrow \gamma_j$ or electron positions $\vec{r}_i \leftrightarrow \vec{r}_j$ will lead to a sign change, and that any wave function containing two elements of identical position and quantum numbers will be zero. Thus, the central-field approximation facilitates a formulation of the wave function that by its nature obeys the symmetries described above.

3.2.2 Configuration state functions

Though the Slater determinant form of the wave function (3.13) gives us a useful tool for finding approximate solutions to the Dirac equation, it has a key weakness. Unlike the exact wave functions, the determinant ones are not necessarily eigenfunctions of the total angular momentum operators [17, p. 12]. In the theory of GRASP, this is solved by formulating wave functions as linear combinations of Slater determinants, built up of wave functions from within the same subshell, i.e. with the same principal and total angular momentum quantum numbers and parity, called *configuration state functions*, or *CSFs* [17, p. 12].

$$\Theta(\vartheta J M_J \pi; \boldsymbol{R}) = \sum_i \Phi(\Gamma_i; \boldsymbol{R}) \quad (3.14)$$

Where π indicates the parity of the wave function, and ϑ the quantum numbers of the state. Now, in multiconfigurational Dirac-Hartree-Fock theory, this goes one step further. The so-called *atomic state function*, or *ASF*, is a linear combination of CSFs[18]

$$\Omega(\omega J M_J \pi; \boldsymbol{R}) = \sum_{k=1}^{N} CF c_k^{\omega J} \Theta(\vartheta_k J M_J \pi; \boldsymbol{R}) \quad (3.15)$$

With ω this time representing all quantum numbers not otherwise specified.

Generating the CSFs

In the GRASP suite, the generation of configuration states is handled by the RCSFGENERATE program. In any computational project, and especially large and/or complex ones, a key goal should be to maximise computational accuracy while minimizing computational cost. The user-defined limitations on the generation of CSFs, as well as the removal of unimportant ones, are the main tools used to achieve this. The generation of CSFs is easily limited, as the user defines for each calculation which electron orbitals are to be taken into account, as well as to what degree excitations between orbitals occur, and the symmetry properties of the resultant ASF. These parameters afford the user a high degree of freedom in how large an expansion ends up being.

Removing CSFs from the generated list

GRASP includes a program, RCSFINTERACT, which looks through a generated list of CSFs, and compares it with a user-defined reference, called the multireference (MR), removing any configuration for which the following holds

$$\langle \mathrm{MR}|\mathcal{H}|\mathrm{CSF}\rangle = 0 \tag{3.16}$$

The Hamilton operator either being the Dirac-Coulomb Hamiltonian, or as will be the case for the present work, the Dirac-Coulomb-Breit Hamiltonian, given by

$$\begin{aligned}\mathcal{H}_{DCB} = \sum_i [\alpha_f^{-1}\vec{\alpha}_i \cdot \vec{p}_i + \alpha_f^{-2}(\beta_i - I_{4\times 4}) + V_{av}(r_i)] \\ - \sum_{j>i=1}^{N} \frac{1}{2r_{ij}} \left[(\vec{\alpha}_i \cdot \vec{\alpha}_j) + \frac{(\vec{\alpha}_i \cdot \vec{r}_{ij})(\vec{\alpha}_j \cdot \vec{r}_{ij})}{r_{ij}^2} \right]\end{aligned} \tag{3.17}$$

Where the first sum is the central-field Hamiltonian presented in equation (3.6), and the second sum accounts for the coupling between spins and orbital motion in the atomic system. The latter is also known as the *Breit interaction*, and is what the *transverse-photon interaction* reduces to in the long-wavelength limit.

The selective generation and removal of CSFs from the calculations are the basis for what is known as the *active set approach*, which will be discussed at length in chapter 7.

Chapter 4

The self-consistent calculation

4.1 The multiconfigurational Dirac-Hartree-Fock method

In the present work, we will follow along with the broad strokes of the derivations of the Hartree-Fock equations presented by I. Lindgren and A. Rosén in an article published in "Case Studies in Atomic Physics" in 1974 [16]. For the omitted steps, the reader is referred to the original work. As a primer before delving into the mathematics of it: the Hartree-Fock equations are found by minimizing the total energy expression with respect to the radial parts P and Q of the wave functions (3.9).

4.1.1 The energy expression

Starting with the exact Dirac-Coulomb Hamiltonian

$$\begin{aligned}\mathcal{H}_{DC} &= \sum_i f_i + \frac{1}{2}\sum_{i,j} g_{ij} \\ &= \sum_i \left(\alpha_f^{-1}\vec{\alpha}_i \cdot \vec{p}_i + \alpha_f^{-2}(\beta_i - I_{4\times 4}) - \frac{Z}{r_i} \right) + \frac{1}{2}\sum_{i,j}\frac{1}{r_{ij}} \end{aligned} \quad (4.1)$$

and the Slater determinant of (3.13), we get the following expression for the total energy of the atomic system

$$E = \langle \Phi | \mathcal{H}_{DC} | \Phi \rangle = \sum_i \langle \phi_i | f | \phi_i \rangle + \frac{1}{2}\sum_{i,j} \left[\langle \phi_i \phi_j | g | \phi_i \phi_j \rangle - \langle \phi_i \phi_j | g | \phi_j \phi_i \rangle \right] \quad (4.2)$$

This can be rewritten in terms of three integrals: one, I_i, involving a single electron, and two, J_{ij} and K_{ij}, involving two electrons

$$E = \sum_i I_i + \frac{1}{2}\sum_{i,j}\big[J_{ij} - K_{ij}\big] \tag{4.3}$$

Where the one-electron integral is given by [16, p. 101]

$$I = \langle\phi|f|\phi\rangle = \int\bigg[cP\bigg(\frac{dQ}{dr} - \frac{\kappa}{r}Q\bigg) - \alpha_f^{-1}Q\bigg(\frac{dP}{dr} + \frac{\kappa}{r}P\bigg) - 2\alpha_f^{-2}Q^2 - \frac{Z}{r}\big(P^2+Q^2\big)\bigg]dr \tag{4.4}$$

and the two-electron integrals are on the form [16, p. 101]

$$\langle\phi_a\phi_b|r_{ij}^{-1}|\phi_c\phi_d\rangle = \sum_{kq}(-1)^q R^k(abcd)\langle\phi_a|C_q^k|\phi_c\rangle\langle\phi_b|C_{-q}^k|\phi_d\rangle \tag{4.5}$$

with $abcd = abab$ for J_{ij}, and $abcd = abba$ for K_{ij}. In the expression above, C_q^k is a tensor related to spherical harmonics[1], and $R^k(abcd)$, called a Slater integral, is given by

$$\begin{aligned} R^k(abcd) &= \int\int \frac{r_<^k}{r_>^{k+1}}\big[P_a(r_1)P_c(r_1) + Q_a(r_1)Q_c(r_1)\big] \\ &\quad\times\big[P_b(r_2)P_d(r_2) + Q_b(r_2)Q_d(r_2)\big]dr_1dr_2 \\ &= \int\frac{1}{r_2}Y_k(ac,r_2)\big[P_b(r_2)P_d(r_2) + Q_b(r_2)Q_d(r_2)\big]dr_2 \end{aligned} \tag{4.6}$$

where

$$\frac{r_<^k}{r_>^{k+1}} = \frac{\min(r_1,r_2)^k}{\max(r_1,r_2)^{k+1}} \tag{4.7}$$

and the function

$$Y_k(ac,r_2) = r_2\int\frac{r_<^k}{r_>^{k+1}}\big[P_a(r_1)P_c(r_1) + Q_a(r_1)Q_c(r_1)\big]dr_1 \tag{4.8}$$

is introduced for the sake of future convenience.

Since the matrix elements with C_q^k in (4.5) only depend on the angular properties of the wave functions, they can be rewritten as the *angular coefficients*

[1] The $\boldsymbol{C}$-tensor, as defined in "Atomic Many-Body Theory" is given by the following relation

$$C_q^k = \sqrt{\frac{4\pi}{2k+1}}Y_q^k(\theta,\varphi)$$

where $Y_q^k(\theta,\varphi)$ are spherical harmonics.

of the energy expression, $C(abk)$ for J_{ij} and $D(abk)$ for K_{ij}. The total energy expression can thus be formulated in terms of the one-electron integral, the angular coefficients, and the Slater integrals as

$$E = \sum_a q_a \left[I_a + \frac{1}{2} \sum_{b,k} \left[C(abk) R^k(abab) + D(abk) R^k(abba) \right] \right] \tag{4.9}$$

where the summations have been nested to highlight the fact that each term in a corresponds to the total energy of the q_a electrons in a subshell defined by nlj. Assuming, of course, that all electrons within an orbital have the same energy.

To derive the Hartree-Fock equations, the total energy (4.9) must be minimized with respect to P and Q. This approach is based on the variational method, so a brief introduction to that approximation method is in order before moving on.

4.1.2 The variational method

In the most general terms, the variational method is based on the fact that for a bound state f, the energy functional

$$\mathcal{E}(f) = \frac{\langle f|\mathcal{H}|f\rangle}{\langle f|f\rangle} \tag{4.10}$$

should be stationary in variations $f \to f + \delta f$. By now looking for functions that satisfy this condition, as well as requiring that

$$\langle f + \delta f | f + \delta f \rangle = 1 \tag{4.11}$$

we get an *optimization problem under the normalization constraint*. This problem can be solved by use of the following theorem [17, p. 14]

> If f is a solution to the optimization problem under the normalization constraint, then there exists a so called *Lagrange multiplier* λ such that the functional
>
> $$\mathcal{F}(f) = \mathcal{E}(f) + \lambda \langle f|f\rangle \tag{4.12}$$
>
> is stationary to first order with respect to *all* variations δf in f satisfying the boundary conditions.

To approximate wave functions using this theorem, one may define the functional on the left-hand side not in terms of the wave function f, but rather in terms of the set of parameters $\boldsymbol{\eta} = \{\eta_1, \eta_2, \ldots, \eta_n\}$ on which the wave function depends. Equation (4.12) may also be further generalized by imposing any number of constraint functions $C(\boldsymbol{\eta})$ with corresponding Lagrange multipliers, yielding

$$\mathcal{F}(\boldsymbol{\eta}) = \mathcal{E}(\boldsymbol{\eta}) + \sum_i \lambda_i C_i(\boldsymbol{\eta}) \tag{4.13}$$

With the stationary condition now being that the partial derivatives of the functional with respect to the parameters η_i must be zero:

$$\frac{\partial \mathcal{F}}{\partial \eta_i} = 0, \, \forall \eta_i \tag{4.14}$$

This way of formulating the variational problem opens it up for computational solution, on which the self-consistent calculation is based.

4.1.3 The relativistic Hartree-Fock equations

By now using as our variational function the energy expression E in (4.9), and enforcing the orthogonality conditions

$$N_{ab} = \int \big(P_a P_b + Q_a Q_b\big) dr = \delta_{a,b} \tag{4.15}$$

we end up with the variational equation

$$\Delta\mathcal{E} = \Delta\left[E - \sum_a q_a \epsilon_{aa} N_{aa} - \sum_{a \neq b} q_a q_b \epsilon_{ab} N_{ab}\right] \tag{4.16}$$

where, according to *Koopman's theorem*, the diagonal Lagrange multiplier ϵ_{aa} equals the energy of a single electron in subshell a.

By requiring that the energy functional $\mathcal{E}$ be stationary with respect to variations in P and Q, one ends up with the expression[2]

$$\begin{aligned}\Delta\mathcal{E} = q_a \Delta I_a &+ \frac{1}{2} q_a \sum_k \big[C(aak)\Delta R^k(aaaa) + D(aak)\Delta R^k(aaaa)\big] \\ &+ q_a \sum_{b \neq a, k} \big[C(abk)\Delta R^k(abab) + D(abk) R^k(abba)\big] \\ &- q_a \epsilon_{aa} \Delta N_{aa} - 2 q_a \sum_{b \neq a} q_b \epsilon_{ab} \Delta N_{ab} = 0\end{aligned} \tag{4.17}$$

which for arbitrary ΔP_a and ΔQ_a should be zero. Inserting each of these conditions into (4.17) will give a set of coupled differential equations in P_a and Q_a, the *relativistic Hartree-Fock equations*

[2]The steps in which the expressions for the variations in the one- and two-electron integrals with respect to variations in P and Q are derived have been omitted, as it would only serve to clutter up the text, without giving much additional information. Again, the interested reader is referred to the original text [16]

$$\frac{1}{\alpha_f}\frac{dQ_a}{dr} - \frac{\kappa}{\alpha_f r}Q_a - \frac{Z}{r}P_a + \sum_{b,k}\left[C(abk)P_a\frac{1}{r}Y_k(bb) + D(abk)P_b\frac{1}{r}Y_k ab\right] = \epsilon_{aa}P_a + \sum_{b\neq a} q_b\epsilon_{ab}P_b \quad (4.18)$$

$$-\frac{1}{\alpha_f}\frac{dP_a}{dr} - \frac{\kappa}{\alpha_f r}P_a - \frac{2}{\alpha_f^2}Q_a - \frac{Z}{r}Q_a + \sum_{b,k}\left[C(abk)Q_a\frac{1}{r}Y_k(bb) + D(abk)Q_b\frac{1}{r}Y_k(ab)\right] = \epsilon_{aa}Q_a + \sum_{b\neq a} q_b\epsilon abQ_b \quad (4.19)$$

Solving these equations is handled by two different programs in GRASP. First, RANGULAR determines the angular coefficients $C(abk)$ and $D(abk)$, then RMCDHF iterates upon the wave functions until *self-consistent* solutions for all orbitals have been found, i.e. orbitals which create a potential from which they themselves can be calculated. Note that with the wave functions of the system assumed to be on the ASF form discussed in chapter 3, this method is called the *multiconfigurational Dirac-Hartree-Fock* method.

4.1.4 On the radial grid

The solution of the Hartree-Fock equations (4.18,4.19) is done on a radial grid defined by

$$r_i = RNT\big(e^{H(i-1)} - 1\big) \text{ i=1, ..., NP} \quad (4.20)$$

where the default values are $RNT = (2\cdot 10^{-6})/Z$, $H = 0.05$, and $NP = 590$ [18]. For heavier atoms, such as bismuth, it becomes necessary to expand the grid to encompass more points. In the present work, this was done in two ways: (1) before compiling GRASP, the value of NP was edited in the source code, to $NP = 2990$, and (2) when running the programs, non-default grid parameters were input where possible. These non-default values were $RNT = (1\cdot 10^{-6})/Z$, and $H = 0.01$. On this grid, the program solves the Hartree-Fock equations using methods of finite difference.

4.1.5 Initialization of the self-consistent calculation

The goal of the self-consistent calculations is to iteratively estimate the orbital wave functions based on the central potential in which the orbitals reside. To

begin this process, the program requires some starting potential upon which it can iterate. This starting point is input in the program RWFNESTIMATE. In the case of repeat calculations on the same system, the program allows for previous results to be input as the starting estimate, as indicated in figure (1.1). If that is not the case, for instance when calculating the wave functions of the multireference, or when including a not preciously used subshell, another starting point must be given. GRASP affords the user three options to choose from, those being the Thomas-Fermi potential, and two varieties of screened hydrogenic potentials. The former is based on the minimization of the total energy of the electron cloud as a number-density distribution with the kinetic energy density of a zero-temperature free-electron gas [3, p. 191]. The latter methods, devised by J. C. Slater, determine the electronic wave functions under the assumption that the potential felt by one electron can be modelled as that felt by an electron in a hydrogen-like system with a nucleus of charge $Z - s$, s here being the *screening constant* [19]. In the present project, the Thomas-Fermi approximation was used for the initial estimates of all newly opened subshell, except for the $6h$ subshell, where the basic screened hydrogenic approximation was used, due to the Thomas-Fermi approximation not being successful.

Chapter 5

Configuration interaction

In the final step before calculating the hyperfine structure, some additional terms must be added to the energy expression to account for relativistic and QED effects. With all the information about the CSFs calculated in the previous steps, the CI calculation, handled by RCI, solves the eigenvalue problem [18]

$$\mathcal{H}\vec{c} = E\vec{c} \tag{5.1}$$

where what is included in the Hamiltonian is decided by the user, depending on which effects are to be included, and $\vec{c} = (c_1, c_2, \ldots, c_{NCF})$ is the eigenvector corresponding to the total energy E of the system. The elements c_i are called the mixing coefficients, and are calculated in the RMCDHF routine. Based on this equation, and energy corrections to be discussed, RCI calculates new wave functions, including the relativistic and QED effects, as well as correlation effects

5.1 The Hamiltonian

In the present project, the Hamiltonian used in the CI calculation consists of five terms, corresponding to the aforementioned Dirac- and Coulomb Hamiltonians with the transverse-photon interaction, along with terms introducing self-energy and vacuum polarization, two effects stemming from QED.

$$\mathcal{H} = \mathcal{H}_{Dirac} + \mathcal{H}_{Coulomb} + \mathcal{H}_{TP} + \mathcal{H}_{SE} + \mathcal{H}_{VP} \tag{5.2}$$

In addition to these terms, the program allows for the application of two mass shift corrections, the normal and specific mass shifts. These are, along with the field shift, two of the mechanisms responsible for the isotope shift to be discussed in chapter 6. Due to the magnitude of the mass shift between large isotopes, being proportional to $(A_1 A_2)^{-1}$ [20], this effect will be disregarded in this thesis. The three other corrections will be treated briefly in the next couple of paragraphs.

5.1.1 The transverse photon effect

This effect, which was briefly discussed in chapter three, comes from the exchange of virtual photons due to couplings between the angular momenta of the electrons: spin-(own)-orbit coupling, spin-other-orbit coupling, spin-spin coupling, and orbit-orbit coupling. The latter two only being very small corrections compared to the first two. This effect is in the current project included in the long-wavelength limit, in which it reduces to the Breit interaction, the rightmost term in (3.17). In GRASP, the frequencies of these transverse photons are scaled, "forcing" the interaction into the low-frequency regime. In the present work, the default scaling factor of 10^{-6} was used for all calculations.

5.1.2 Self-energy

The self-energy correction arises due to the fact that the electron may interact with its own electromagnetic field. In the RCI program, the user sets the largest principal quantum number for which the self-energy correction should be applied. In accordance with the user manual [21, p. 35], this value was set to $n = 7$, slightly higher than the highest spectroscopic n.

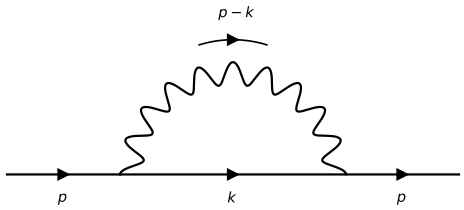

Figure 5.1: Feynman diagram of the self energy interaction of an electron with itself.

The figure above shows the Feynman diagram representation of the electronic self-energy, with the electron emitting a photon which then interacts with the same electron.

5.1.3 Vacuum polarization

The vacuum polarization is the spontaneous creation of a virtual electron-positron pair within the field of the nucleus, i.e. the energy of the nucleus makes the vacuum into a polarizable medium of sorts. Due to the energy required for this to happen, this effect becomes more important when dealing with heavy or superheavy atoms, than when dealing with lighter ones.

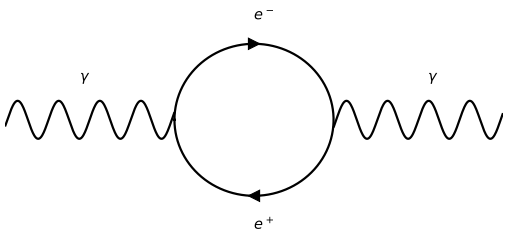

Figure 5.2: Feynman diagram of vacuum polarization; the spontaneous creation of virtual electron-positron pairs in the field of the nucleus.

The figure above shows the Feynman diagram representation of vacuum polarization, with a photon splitting into an electron-positron pair, which promptly annihilates.

Chapter 6

Hyperfine structure

In examining the energy spectrum of an atomic species, one may notice that what at first seemed like unique spectral lines, in fact consist of several, tightly-spaced lines. By looking even closer, one may again notice that these lines can be further split into another set of lines. These new sets of spectral lines are known as the *fine structure* and *hyperfine structure*, in contrast to the original spectrum which is known as the *gross structure* of the atom. The gross atomic structure, as described in chapter 2, stems from the transitions between the distinct stationary states of the atom. The fine structure splitting comes from the couplings of the angular momenta of electrons; that which is included in the Breit interaction. Lastly, hyperfine splitting is an effect stemming from the interactions between the multipole moments of the nucleus and the electrons.

For the remainder of this chapter, hyperfine structure will be given a thorough treatment, using the tensor algebra formulation found in much of the literature upon which the methods used in this thesis are based. The chapter will end with discussions of the isotope shift, the shifting of energy levels for different isotopes, and the hyperfine anomaly, the deviation of theoretically evaluated isotope shifts arising as a consequence of the inaccuracies in the magnetic dipole approximation of the nucleus.

6.1 Tensor operator form of the hyperfine interaction

The hyperfine splitting of energy levels occurs due to multipole interactions between the electrons and the nucleus. As a result, there are two components of this that must be discussed: the electric interaction stemming from the multipole expansion terms of even order, and the magnetic interaction from those of odd. The operator representing the hyperfine interaction can be written as a sum over scalar tensor products [17, p. 165]:

$$\mathcal{H}_{hfs} = \sum_{K \geq 1} \mathbf{T}^{(K)} \circ \mathbf{M}^{(K)} \tag{6.1}$$

Here, $\mathbf{T}$ and $\mathbf{M}$ are tensor operators acting on the electronic and nuclear subsystems, respectively, and "$\circ$" is the general notation for a scalar tensor product.

Luckily, the relative contributions of each new multipole term is less than the previous, meaning that for a discussion of hyperfine structure, only the first two terms are necessary, those being the magnetic dipole interaction ($K = 1$), and the electric quadrupole interaction ($K = 2$) [17, p. 165].

In the usual way, the energy added to a state by the hyperfine interaction can be calculated as the matrix element of said state with the operator (6.1):

$$\begin{aligned} E_{hfs} &= \langle \nu\gamma IJFM_F | \mathcal{H}_{hfs} | \nu\gamma IJFM_F \rangle \\ &= \langle \nu\gamma IJFM_F | \mathbf{T}^{(1)} \circ \mathbf{M}^{(1)} | \nu\gamma IJFM_F \rangle \\ &+ \langle \nu\gamma IJFM_F | \mathbf{T}^{(2)} \circ \mathbf{M}^{(2)} | \nu\gamma IJFM_F \rangle \\ &= E_{M1} + E_{E2} \end{aligned} \tag{6.2}$$

The state in question is defined in terms of the non-angular electronic and nuclear quantum numbers γ, ν, the angular momentum of the electrons, $\mathbf{J}$, the angular momentum of the nucleus, $\mathbf{I}$, and the total angular momentum $\mathbf{F}=\mathbf{I}+\mathbf{J}$.

It is worth noting here that this way of adding the hyperfine interaction hinges on perturbation theory, i.e. the assumption that the effects can be added to the Hamiltonian as a small "perturbative term": $\mathcal{H} = \mathcal{H}_0 + \mathcal{H}'$. This is usually the case if the perturbation is small compared to the original Hamiltonian, which will be justified in the present chapter.

6.1.1 The magnetic dipole interaction

The two $K = 1$ tensors in the hyperfine operator are [17, pp. 165-166]:

$$\begin{aligned} \mathbf{T}^{(1)} = \frac{\alpha_f^2}{2} \sum_{i=1}^{N} \Big[& 2\mathbf{L}_e^{(1)}(i) r_i^{-3} - g_{s,e}\sqrt{10}\big[\mathbf{C}^{(2)}(i) \times \mathbf{S}_e^{(1)}(i)\big] r_i^{-3} \\ & + g_{s,e}\frac{8}{3}\pi\delta(\vec{r}_i)\mathbf{S}_e^{(1)}(i) \Big] \end{aligned} \tag{6.3}$$

for the electronic part, and

$$\mathbf{M}^{(1)} = \mu_N \sum_{i=1}^{\text{nucleons}} \nabla\big(r_i \mathbf{C}^{(1)}(i)\big) \cdot \big[g_{l,n}\mathbf{L}_e^{(1)}(i) + g_{s,n}\mathbf{S}_e^{(1)}(i)\big] \tag{6.4}$$

for the nucleonic.

In the first equation, (6.3), $g_{s,e} \approx 2.00232$ is the electronic g-factor , $\mathbf{L}_e$ and $\mathbf{S}_e$ are the orbital and spin angular momentum operators of the electrons, and $\mathbf{C}^{(2)}$ is the $\mathbf{C}$-tensor of rank 2, and $\delta(\vec{r}_i)$ is the Dirac delta-function. The three terms in the sum represent three different physical mechanisms. The first term is called the *orbital term*, and represents the field generated by the orbital motion of the electrons. The second term, the *spin-dipole term* represents the field generated by the electron spins. Lastly, the third term, also known as the *Fermi contact term*, represents the contact interaction between the nucleus and the electrons, and is proportional to the spin-density at the nucleus [17, pp.165-166]. This last effect is the origin of the aforementioned significance of the s and $p_{1/2}$ orbitals, which overlap the nucleus, and is thus responsible for the Breit-Rosenthal effect, i.e. the effect on the hyperfine spectrum of the nucleus having an extended charge distribution, rather than being point-like.

On to the second equation, (6.4). We have $g_{l,n}$ and $g_{s,n}$, being the orbital and spin g-factors of the nucleons, and $\mathbf{L}_n$ and $\mathbf{S}_n$ the orbital and spin angular momentum operators of the nucleons, as well as the rank-one $\mathbf{C}$-tensor.

The magnetic dipole hyperfine constant

By looking at the dependence of the magnetic dipole energy on the quantum number F, we can quite elegantly derive an expression for the *magnetic dipole hyperfine constant*, a scaling factor connecting the differently coupled $\mathbf{I}$ and $\mathbf{J}$ states to the resulting hyperfine energy levels. Using some tensor algebraic identities [1], the F-dependency of the magnetic dipole contribution to the hyperfine energy can be shown to be [22, p. 339]

$$\begin{aligned} E_{M1} &= \langle \gamma \nu I J F M_F | \mathbf{T}^{(1)} \circ \mathbf{M}^{(1)} | \gamma \nu I J F M_F \rangle \\ &= (-1)^{I+J+F} \begin{Bmatrix} I & J & F \\ J & I & 1 \end{Bmatrix} \langle \gamma J || \mathbf{T}^{(1)} || \gamma J \rangle \langle \nu I || \mathbf{M}^{(1)} || \nu I \rangle \end{aligned} \tag{6.5}$$

Where the expression in the braces is the Wigner 6-j symbol. Using the exact same relation on the scalar product $\mathbf{I} \cdot \mathbf{J}$, we get:

$$\langle I J F M_F | \mathbf{I} \cdot \mathbf{J} | I J F M_F \rangle = (-1)^{I+J+F} \begin{Bmatrix} I & J & F \\ J & I & 1 \end{Bmatrix} \langle J || \mathbf{J} || J \rangle \langle I || \mathbf{I} || I \rangle \tag{6.6}$$

Since the F-dependencies are clearly the same, the dipole operator can be rewritten as

$$\mathcal{H}_{dip} = \mathbf{T}^{(1)} \circ \mathbf{M}^{(1)} = A(\mathbf{I} \cdot \mathbf{J}) \tag{6.7}$$

with [22, p. 339][17, p. 168]

[1] The identities in question are the Wigner-Eckart theorem, and the Wigner 3n-j symbols. For anyone interested, [22], [23], and [7] give good introductions to the application of tensor algebra to atomic systems.

$$A = \frac{\langle \gamma J||\mathbf{T}^{(1)}||\gamma J\rangle\langle \nu I||\mathbf{M}^{(1)}||\nu I\rangle}{\langle J||\mathbf{J}||J\rangle\langle I||\mathbf{I}||I\rangle}$$
$$= \frac{\mu_I}{I}\big[J(J+1)(2J+1)\big]^{-1/2}\langle \gamma J||\mathbf{T}^{(1)}||\gamma J\rangle \quad (6.8)$$

This "A", with units of frequency, is called the *dipole interaction constant*, or the *magnetic dipole hyperfine constant*. Notice that the magnetic dipole moment has appeared in the equation above, as hinted at in chapter 3.

It is worth noting that equation (6.8) is only valid for diagonal matrix products [22, p. 339]. The RHFS program in GRASP also calculates the off-diagonal hyperfine constants $A_{J,J-1}$, though these will not be of use in the present project. The expressions and energy shifts for these off-diagonal elements can be found in [24].

By simple algebraic manipulation, the scalar product in (6.7) can be rewritten in terms of the eigenvalues of $\mathbf{I}$, $\mathbf{J}$, and $\mathbf{F}$:

$$\mathbf{F} = \mathbf{I} + \mathbf{J} \quad (6.9)$$
$$\Rightarrow \mathbf{F}^2 = \mathbf{I}^2 + \mathbf{J}^2 + 2\mathbf{I}\cdot\mathbf{J} \quad (6.10)$$
$$\Rightarrow \mathbf{I}\cdot\mathbf{J} = \frac{1}{2}(\mathbf{F}^2 - \mathbf{I}^2 - \mathbf{J}^2) \quad (6.11)$$

Which, when inserting the standard eigenvalues of angular momentum operators, yields:

$$E_{M1} = A(\mathbf{I}\cdot\mathbf{J}) = \frac{1}{2}A\big[F(F+1) - I(I+1) - J(J+1)\big] \quad (6.12)$$

From the equation above it is also clear that the energy difference due to the magnetic dipole interaction between the two states $|\gamma\nu IJFM_F\rangle$ and $|\gamma\nu IJ(F-1)M_F\rangle$, must be AF.

Example I: Magnetic dipole hyperfine splitting in the $^4S^o_{3/2}$ state of ^{209}Bi

As an illustration of this effect, consider the unperturbed spectral line for the ground state $^4S^o_{3/2}$ of ^{209}Bi. According to experimental data tabulated by Wilman, Ruczkowski, and Elantkowska, this state has a hyperfine constant $A_0 = 446.937(1)$ MHz [25]. The nuclear angular momentum of ^{209}Bi is $I = 9/2$, and the electronic angular momentum of the state in question is $J = 3/2$. The allowed values of F lie within the interval $[|i-j|, i+j]$, which in this case means $F \in \{3, 4, 5, 6\}$, giving four distinct hyperfine levels: $A_0 - 4134.167$ MHz, $A_0 - 2346.419$ MHz, $A_0 - 111.734$ MHz, and $A_0 + 2569.888$ MHz.

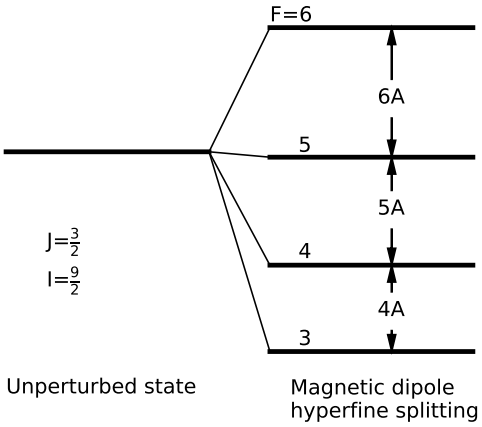

Figure 6.1: The magnetic dipole hyperfine levels of the ${}^4S^o_{3/2}$ state of ^{209}Bi.

Though the range spanned by the hyperfine levels may seem large, translating it into a more "intuitive" form using the standard result $E = h\nu$, ν being frequency and h the Planck constant, shows that the levels are separated by at most 28 μeV. Not a large effect compared to the gross atomic structure, with line separations typically measured in eV. This is also why, as mentioned above, perturbation theory is applicable to hyperfine interactions; the relative change in energy is usually very small.

6.1.2 The electric quadrupole interaction

The other main contributor to hyperfine level splitting, is the interaction between the electric quadrupole moments of the electron orbitals and the atomic nucleus. The operators of (6.1) with K=2, are [17, pp. 165-166]:

$$\mathbf{T}^{(2)} = -\sum_{i=1}^{N} \mathbf{C}^{(2)}(i) r_i^{-3} \tag{6.13}$$

and

$$\mathbf{M}^{(2)} = \sum_{i=1}^{\text{protons}} r_i^2 \mathbf{C}^{(2)}(i) = \sum_{i=1}^{\text{protons}} (3z_i^2 - r_i^2) \tag{6.14}$$

Notice in the nuclear quadrupole term (6.14) that the sum is only over the protons in the nucleus, whereas the dipole term (6.4) contained a sum over all nucleons.

The electric quadrupole hyperfine constant

In the same manner as the magnetic dipole hyperfine constant, there exists an electric quadrupole hyperfine constant B. With the same diagonality restriction as for the magnetic dipole hyperfine constant, the electric quadrupole hyperfine constant can be written [17, p. 168]:

$$B = 2Q\left[\frac{J(2J-1)}{(J+1)(2J+1)(2J+3)}\right]^{1/2}\langle\gamma J||\mathbf{T}^{(2)}||\gamma J\rangle \tag{6.15}$$

Where Q is the nuclear electric quadrupole moment, which for ^{209}Bi is $Q = -0.516(15)$ b[12]. The energy shift due to the this interaction can be written as [17, p. 168]:

$$E_{E2} = B\frac{\frac{3}{4}C(C+1) - I(I+1)J(J+1)}{2I(2I-1)J(2J-1)} \tag{6.16}$$

With $C = F(F+1) - I(I+1) - J(J+1)$. In the same manner as for A, GRASP calculates the off-diagonal hyperfine constants $B_{J,J-1}$ and $B_{J,J-2}$ [24].

Example II: Electric quadrupole hyperfine splitting in the $^4S^o_{3/2}$ state of ^{209}Bi

By again looking at the $^4S^o_{3/2}$ state, and using the value $B = 305.067(2)$ MHz from the aforementioned article [25], we find that the electric quadrupole interaction shifts the spectral lines in figure 6.1 by at most 140 MHz, so only a small change compared to the magnetic dipole splitting. In units of energy, the electric dipole interaction at most shifts the spectral lines by approximately 0.5 μeV.

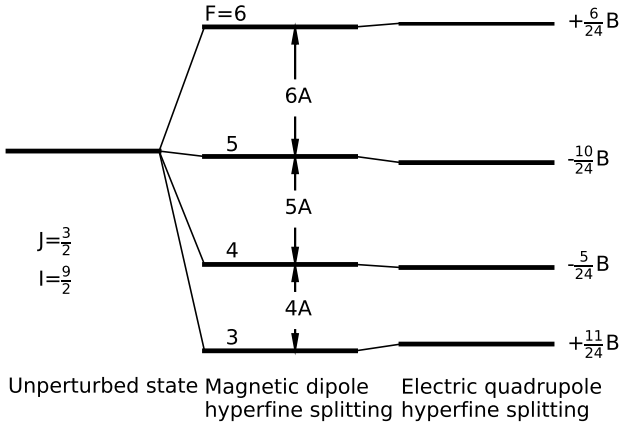

Figure 6.2: The electric quadrupole hyperfine levels of the $^4S^o_{3/2}$ state of ^{209}Bi.

As the figure shows, the splitting due to the electric quadrupole interaction is less significant than the magnetic dipole interaction, for this state.

6.1.3 Higher-order multipole terms

Now, it is obvious that the electric quadrupole interaction contributes far less to the hyperfine splitting than does the magnetic dipole interaction, negating the need for including the next electric term, the electric hexadecapole term. It is not so obvious that the next magnetic one, the octupole term, can excluded, as even though it contributes less than the dipole interaction, there is no guarantee that the octupole interaction will be negligible. For that, we may look to the literature. According to an atomic-beam magnetic-resonance measurement carried out by Hull and Brink, the hyperfine line separations in the ground state of ^{209}Bi are $\Delta E_{3\to4} = 1584.502(2)$ MHz, $\Delta E_{4\to5} = 2171.419(2)$ MHz, and $\Delta E_{5\to6} = 2884.666(2)$ MHz [26]. The subscripts indicate the values of F the line separations are measured between. With the energies calculated using (6.12) and (6.16), we get $\Delta E^{(calc)}_{3\to4} = 1584.370$ MHz, $\Delta E^{(calc)}_{4\to5} = 2171.130$ MHz, and $\Delta E^{(calc)}_{5\to6} = 2885.000$ MHz. Comparing these values to those of Hull and Brink, we see that even with only the first two terms in the multipole expansion included, the values are within approximately 0.01% of the experimentally measured values for the hyperfine line distances of the $^4S^o_{3/2}$ state[2]. Higher-order terms might be necessary when dealing with deformed nuclei, as higher degrees of asymmetry will lead to larger multipole moments. These nuclei are generally found in the ranges $A < 190$ and $A > 220$, and so this does not apply to most bismuth isotopes.

6.2 Isotope shift

When comparing the atomic spectra of two isotopes of the same element, the lines will not match exactly; there will be a shift in the energy levels between isotopes. This shift is typically separated into two separate mechanisms, the mass shift and the field shift, also known as the mass effect and the volume effect.

6.2.1 Mass shift

As mentioned briefly in the previous chapter, the mass shift is really the combined effect of two mechanisms. The normal mass shift, and the specific mass shift. As given by Cowan, the kinetic energy of an N-electron atom with a nucleus of mass M is [3, p. 505]

[2]Note that the thesis concerns itself with not just the ground state, but also the states $^2P^o_{1/2}$, $^2D^o_{3/2}$, $^2P^o_{3/2}$, and $^2D^o_{5/2}$. Though $^4S^o_{3/2}$, being the ground state, is used as a benchmark for the system as a whole.

$$E = \sum_i \frac{p_i^2}{2\mu} + \frac{1}{M}\Big(\sum_{i<j} \vec{p}_i \cdot \vec{p}_j\Big) \tag{6.17}$$

where $\mu = Mm_e/(M + m_e)$ is the reduced mass of the atom (m_e is included here for clarity). The first of these two effects is the normal mass shift, and the second the specific mass shift. By using this equation, it is easy to show that when comparing isotopes of masses M, M', these two effects will both be proportional to $(M' - M)/MM'$. In the case of bismuth, the numerator in this expression will typically be < 20 amu, while the denominator will be $> 40\ 000$ amu^2. For that reason, the mass shifts will not be included in the present work. In general, the mass shift becomes less significant (and the field shift more so), for the heavier atoms. According to Rudzikas, the mass shift can be neglected around Z=60 [7, p. 269].

6.2.2 Field shift

The field shift, also known as the *volume shift*, is the isotopic shift of interest to the present work. When we go from a description of the atomic nucleus as an infinitesimal point charge to an extended charge distribution, the potential felt by the electrons will change. Specifically, where the electron orbitals overlap with the nucleus, the electrons will feel a smaller potential, due to them now being inside the charge distribution. Since the addition or subtraction of nucleons will affect the geometry of the nucleus, the energy levels of separate isotopes will be shifted due to this effect. This shift is proportional to the electron density at the centre of the nucleus, as well as the mean squared charge radius of the nucleus [17, p. 158]:

$$E^{fs} = \frac{2\pi}{3} Z \rho_e(\vec{0}) \langle r^2 \rangle \tag{6.18}$$

where Z is the atomic number, $\rho_e(\vec{0})$ is the electronic charge density at the nuclear centre[3], and $\langle r^2 \rangle$ is the mean squared charge radius of the nucleus. Comparing equations (6.17) and (6.18), we see that as we go towards larger, and thus heavier atoms, the mass shift becomes less important, while the significance of the field shift only grows. The fact that the field shift is linear in $\langle r_M^2 \rangle$ allows for the isotope shift, and the closely related Breit-Rosenthal effect[4] to be estimated using simple linear regression.

[3] The derivation is based on the assumption that electronic charge distribution varies little over typical nuclear distances, and as such can be set equal to its value at the centre.

[4] As will be discussed, the Breit-Rosenthal effect also arises due to the volume effects of a non-pointlike nucleus, and can therefore also be expected to be linear in $\langle r^2 \rangle$.

6.3 Corrections to the magnetic dipole hyperfine constant

With the relative contributions of the multipole terms established, it is time to take a look at some corrections to the largest contributor - the magnetic dipole interaction.

The model of the nucleus as a point dipole, a current loop of infinitesimal physical extent, is a mathematical approximation. The real nucleus is a quantity with both an extended charge distribution, as discussed in chapter 2, and an extended current distribution, i.e. magnetization. These two properties of the nucleus will displace the spectral lines calculated in the point dipole approximation above, (6.12).

6.3.1 The Breit-Rosenthal effect

The former of the two aforementioned effects was first described in an article published by Jenny Rosenthal and Gregory Breit in 1932[5], after whom the effect is named[6]. Based on the observation that the isotope shifts seen in experiments differed by theoretical calculations in such a way as to not be explainable by the mass shift, they found that the shifts could be explained by modifying the nuclear electric field from that of the simple Coulomb law. They also showed that this effect was mainly due to s electrons, and that the shift was roughly proportional to the probability of finding an electron in the nuclear centre, $|\Psi(\vec{0})|^2$ [27]. Due to the fact that the overlap of the electrons with the nucleus will serve to lower the potential felt by said electrons, the Breit-Rosenthal correction should reduce the magnetic dipole hyperfine constant for isotopes with larger mean squared charge radii.

6.3.2 The Bohr-Weisskopf effect

As this effect is not the focus of this thesis, it will only be treated briefly. In the same manner as done by Breit and Rosenthal almost two decades earlier, Aage Bohr[7] and Victor Weisskopf sought to explain another discrepancy in isotope shifts. They found that the distribution of the magnetizations of different isotopes could affect their spectra, similar to the distribution of charge in the Breit-Rosenthal case [29]. Since the field line density of a perfect dipole will be higher than that of a physical dipole, the Bohr-Weisskopf effect will also lead to a lowering of the magnetic dipole hyperfine constant.

[5] Amusingly, the paper ends with a note about how, after writing the paper, the authors were informed of Heisenberg's new theory that "the nucleus is supposed to consist of protons and neutrons" [27].

[6] The effect may also be found in the literature as the Breit-Rosenthal-Crawford-Schawlow effect, with the latter researchers credited with experimentally verifying Breit-Rosenthal's results [28].

[7] Niels' son.

6.3.3 The hyperfine anomaly

The two "non-dipole" corrections can both be applied to the magnetic dipole hyperfine constant as simple multiplicative factors [30]:

$$A' = A_p(1 + \epsilon_{BW})(1 + \epsilon_{BR}) \tag{6.19}$$

Where A_p is the hyperfine constant of a point charge nucleus, and the subscripts on the corrective ϵ factors refer to the **B**ohr-**W**eisskopf and **B**reit-**R**osenthal effects. In comparing two isotopes, the quantity of interest will be the ratio of two magnetic dipole hyperfine constants:

$$\frac{A'_1}{A'_2} = \frac{\mu_1/I_1}{\mu_2/I_2} \frac{(1 + \epsilon^{(1)}_{BW})(1 + \epsilon^{(1)}_{BR})}{(1 + \epsilon^{(2)}_{BW})(1 + \epsilon^{(2)}_{BR})} \tag{6.20}$$

Where the quantity μ/I is also known as the gyromagnetic ratio g_l.

By working with the assumption that the Bohr-Weisskopf and Breit-Rosenthal effects are small, this can be rewritten in terms of the differential quantities ${}^1\Delta^2 = \epsilon^{(1)} - \epsilon^{(2)}$:

$$\frac{A'_1}{A'_2} \approx \frac{\mu_1/I_1}{\mu_2/I_2}(1 + {}^1\,\Delta^2_{BW})(1 + {}^1\,\Delta^2_{BR}) \tag{6.21}$$

If, as is often the case, one of the effects dominates, only that effect need be included, and the subscripts can be dropped:

$$\frac{A'_1}{A'_2} \approx \frac{\mu_1/I_1}{\mu_2/I_2}(1 + {}^1\,\Delta^2) \tag{6.22}$$

Where the differential ${}^1\Delta^2$ now describes the hyperfine anomly in its entirety. Looking back at the first equation of this thesis (1.1), we see that quantifying the hyperfine anomaly allows for the application of a corrective factor to the calculated magnetic dipole moment.

The quantity of interest in this study, is the Breit-Rosenthal correction, which will be quantified on the form

$${}^1\Delta^2_{BR} = \lambda\delta\langle r^2\rangle_{1,2} \tag{6.23}$$

With $\delta\langle r^2\rangle_{1,2}$ being the difference in mean squared charge radius between isotopes 1 and 2.

Chapter 7

Active set approach

When doing calculations on large, complicated systems, such as ^{209}Bi, there are in principle two ways to approach the issue. One is to feed an arbitrarily large dataset into a supercomputer, allowing it to crunch the numbers for however long it needs. The amount of time such a calculation requires might be on the order of hours, or it might be on the order of days, months, or years, if at all possible. Such computational times are obviously not ideal, nor necessarily possible, depending on the time allotted to a project. In addition to this being a waste of the researcher's time, and other's time if the calculation is run on a shared mainframe, it also wastes a lot of energy, all to compute every minute, unimportant detail of the system.

The other, more sensible method, which is used in this project, is to do a preliminary exploration of the system, to figure out which parts are important, and which can be discarded. The drawbacks of this strategy are mainly the increased complexity of the calculations, and the extra time it takes to do the preliminary exploration. However, the larger and more complex a system is, the more this time pays off.

As mentioned in chapter three, the main avenue for researcher control when it comes to computational resources, is in the number of configuration states generated. In what is known as the *active set approach*, the orbitals of the atom are systematically evaluated in terms of their contribution to the calculated hyperfine constant, with unimportant orbitals being excluded from the calculation.

7.1 Spectroscopic and virtual orbitals

In GRASP, the orbitals of the *active set* are separated into two main categories: the *spectroscopic orbitals* which make up the so-called *multireference* (MR) of the system, and the *virtual orbitals* to which excitations from the spectroscopic orbitals are allowed. Since the spectroscopic orbitals are selected from those orbitals which are occupied in the ground state, they are also referred to as *core*

orbitals. Similarly, since the virtual orbitals are used to calculate correlation energies, they are also known as *correlation orbitals*. When generating the list of CSFs with RCSFGENERATE, the user gives a set of limitations to the system, those being which core orbitals are active, which spectroscopic orbitals are active, how many excitations may occur between them, and what the total angular momentum of the resultant state should be. If all possible CSFs resulting from N excitations between the spectroscopic and virtual sets are generated, the resulting expansion is called a *complete active space* (CAS). If, on the other hand, some restriction is placed upon the generation of CSFs, one is using a *restricted active space* (RAS). In this chapter, the use of both complete and restricted active spaces will be examined, with the accuracy and computational strain resulting from both being a key aspect of the methods chosen.

7.2 Choosing a multireference

As mentioned in chapter three, an important part of limiting the computational cost of a calculation, is the removal of relatively unimportant CSFs from the active space. To do that, the matrix element from (3.16) is calculated, and all CSFs that yield zero, are removed. The bra-function in (3.16) is the ASF for the multireference (MR), which will be discussed presently.

When selecting the MR, it is common to include all closely-degenerate states, to improve the accuracy of the results [21, p. 40]. In the case of ^{209}Bi, one could for instance start with the valence subshells $6s^26p^3$, and then expand the multireference by also including the configurations $6s6p^36d$ and $6s^26p^27p$. These specific examples are based on an exploration of the MR, done in the current work, using the program RCSFMR. Due to issues with achieving convergence for any expanded MR, however, only the first of the three configurations mentioned above was included [1]. These convergence issues also arose when attempting to do calculations on even-parity states. This will be discussed further in chapter 10.

7.3 Excitations/substitutions

When improving the ASF, lists of CSFs are generated where, in addition to the MR, excitations are allowed from spectroscopic orbitals to virtual ones, as discussed above. When generating the list of configurations, the user inputs the allowed number of excitations, which RCSFGENERATE uses to generate all permutations of electrons within the user-set limits. In the present project single (S), double (D), and triple (T) excitations will be used. Note that when double excitations are input, the program generates all electron configurations possible with both single and double excitations. For that reason, double excitations

[1] Chapter 13 of the GRASP user manual [21, pp. 271-298] outlines some methods for achieving convergence. Of these, all except running the programs with non-default options were attempted. The results acquired with only the ground state valence shells were accurate enough so as to not create the need for further attempts at expanding the MR

will be denoted SD, and triple excitations SDT. In addition, the letter "r" will be used to indicate restricted excitations.

7.3.1 Correlation interactions

By improving the ASF with additional CSFs created by excitations from the MR, one includes correlation effects into the energy expression of the system. The correlation effects can be separated into two groups, those arising from single excitations, and those from double.

Single excitations - polarization effects

Due to the pairing of electrons in filled subshells, the spin-density at the nucleus will be zero from a closed electron subshell, in the central-field approximation, leading to the contact term in (6.3) vanishing. Were the valence electrons to generate a field to "pull apart" the spin-up and spin-down electrons within filled subshells, the spin-density would no longer be zero, and a contact interaction would occur. This *spin polarization* effect is emulated in the GRASP package by single excitations from core subshells. Due to this, most of the hyperfine interaction is accounted for using single excitations. There is also an effect arising due to the valence shell distorting the spherical symmetry of closed subshells, called "orbital polarization", though the effect of this polarization on the magnetic dipole hyperfine constant is small, compared to that of the spin polarization [17, p. 173]. There is also another type of single-excitation correlation effect, *radial correlation*, stemming from single excitations that only differ from the reference in principal quantum number, retaining the reference's angular coupling [17, p. 70]. Due to only the polarization effects being treated in [17] with regards to their effect on the hyperfine structure, radial correlation will not be discussed further here.

Double excitations - correlation effects

The correlation effects arising from double excitations are sorted into three groups, based on which orbitals are being excited. In *valence correlation*, excitations only occur from the valence subshells, in *core-valence correlations*, one excitation is from a core subshell and one from a valence subshell, and in *core-core correlation* both excitations come from core subshells.

7.4 A word on notation

Before delving in to the actual calculations, a quick word on notation might be of use. In the literature surrounding GRASP, there are several shorthands for describing the active set of orbitals. In this thesis, the following are adopted: the subset containing spectroscopic orbitals will be described by principal and angular momentum quantum number. In this notation, $6sp5spd$ refers to two orbitals in the sixth shell, $6s$, $6p$, and three orbitals in the fifth, $5s$, $5p$, $5d$.

For virtual orbitals, the scheme used by Bieroń and Pyykkö [31] was found to be most practical, in which virtual layers are described in terms of how many orbitals of each symmetry are included. In this notation, for ^{209}Bi, $2spd1f$ would refer to the set {5f,6d,7s,7p,7d,8s,8p}, i.e., the set of virtual orbitals containing two orbitals each of symmetries $l = s, p, d$, and one orbital with symmetry $l = f$. Beware that some authors use a similar notation, but with the total number of orbitals of each symmetry in the active set included, not just those in the virtual subset.

When the active spaces are described in the next chapter, relativistic subshells are not indicated, as the non-relativistic notation is used in GRASP for including (or excluding) subshells. The relativistic subshells are implicit, so to say.

Chapter 8

Computational methods

In the following, the use of eight different expansion methods of both the complete and restricted active space approaches will be outlined for the calculation of the hyperfine constant in ^{209}Bi. Both due to the size and complexity of the isotope in question, and the large number of repeat calculations for mapping out the dependence of A on variations in mean squared charge radius and skin thickness, limiting expansion size bloat has been a priority in the methods that follow. Of the methods below, three are CAS expansions, and five are RAS expansions. Most of the calculations reported in this project were performed on the high-performance computing (hpc) cluster Idun[32], at the Norwegian University of Science and Technology (NTNU).

8.1 Expanding the active set

The active set was explored in two separate series of calculations, one focused on the systematic expansion of the virtual space, and one on the systematic expansion of the spectroscopic set. Note that, as mentioned in the previous chapter, the multireference used in this project was the simplest one, $6s^2 6p^3$.

8.1.1 Virtual orbitals

The virtual orbitals were opened one by one, and S and/or SD excitations from one or both of the valence shells $n = 5, 6$ were allowed to the entirety of open virtual subshells. At each step, the "outermost[1]" layer of virtual subshells were optimized, and all others kept frozen. Based on this exploration, results not shown, the virtual spaces appropriate for single excitations were on the form $Nspdf$, whereas for expansions including double excitations, g- and h-orbitals had to be included, giving the active spaces $Nspdfg1h$. Note that with $l = h$, only the orbital with $n = 6$ had to be included.

[1] Defined by the highest azimuthal quantum number l for each principal quantum number n

8.1.2 Spectroscopic orbitals

The spectroscopic orbitals, too, were opened one at a time, now allowing for excitations up to the virtual space spanned by four virtual layers on the form $Nspdfg1h$. At each step, the core orbitals were optimized only in the MR calculation, and kept frozen when the virtual layers were added. The virtual layers were optimized as described above. Based on these explorations, the orbitals $1s2sp3d$ were excluded[2], all other orbitals were included. For each of the methods described below, the spectroscopic set was expanded in steps, wherein all orbitals in the same shell were included simultaneously.

8.2 The methods

Eight different methods of expanding the active set were examined in this project. Three were CAS expansions based on S, SD, and SDT expansions. The remaining five were all RAS methods, whereof four were based on the admittedly sparse description of the method used by Bieroń and Pyykkö when calculating the electric quadrupole moment of ^{209}Bi [31].

8.2.1 Methods I-III: Complete active set expansions

In the simplest methods, the expansions were generated by unrestricted S, SD, and SDT excitations. Due to the sizes of the latter two, the expansions of the spectroscopic sets were cut short after the fifth and sixth shells, respectively. The expansions are detailed in the table below, with the total number of CSFs generated in an expansion denoted by *NCF*.

Table 8.1: Summary of the largest expansions of methods I-III.

Mthd.	From	Exc.	To	NCF
I	$6sp5spd4spdf3sp$	S	$4spdf$	6 865
II	$6sp5spd$	SD	$4spdfg1h$	768 994
III	$6sp$	SDT	$4spdf1gh$	771 194

It is worth noting that due to the Dirac-Coulomb-Breit Hamiltonian only containing one- and two-particle operators, the RCSFINTERACT method of removing CSFs was not applicable in method III, which used SDT excitations.

[2]There is a possibility that the calculations could have benefited from the inclusion of the $2s$ orbitals, however, satisfactory results were achieved with only $n = 3, 4, 5, 6$.

8.2.2 Method IV: Restricted SD excitations

Since the majority of the hyperfine interaction is accounted for via single excitations, a way to combat the sharp increase in NCF with adding excitations, is to restrict said excitations in some way. In this method, unrestricted SD excitations were allowed from $6sp$, plus restricted SD excitations from all subshells, wherein at most one excitation at a time could come from the core. The valence $6sp$ subshells were fully open for all excitations. Note that due to these calculations originally being part of the preliminary exploration of the core, the 3s subshell was closed.

Table 8.2: Summary of the the largest expansion of method IV.

Mthd.	From	Exc.	To	NCF
IV	$6sp5spd4spdf3p$	SrD	$4spdfg1h$	714 496

8.2.3 Methods V-VIII: Bieroń-Pyykkö

The method common to all the following methods, is that single excitations are augmented by double excitations from differing subsets of the spectroscopic set.

Table 8.3: Summary of the the largest expansions of methods V-VIII. Configurations only allowing J=3/2 highlighted in bold.

Mthd.	From	Exc.	To	NCF
V	$6sp5spd4spdf3sp$	S	$4spdfg1h$	83 725
	$6sp$	SD	$4spdfg1h$	
	$5spd6sp$	SD	$1spdfgh$	
VI	$6sp5spd4spdf3sp$	S	$4spdfg1h$	41 723
	$6sp$	SD	$4spdfg1h$	
	$6sp5spd$	SrD	$1spdfgh$	
VII	$6sp5spd4spdf3sp$	S	$4spdfg1h$	203 299
	$6sp$	SD	$4spdfg1h$	
	6sp5sp4spd	**SrD**	**4spdfg1h**	
	$6sp5spd$	SrD	$1spdfgh$	
VIII	$6sp5sp4sp3sp2sp1s$	S	$4spdfg1h$	29 389
	$6sp$	SD	$4spdfg1h$	
	$6sp5sp$	SrD	$1spdfgh$	

The one row highlighted in bold type had the additional restriction that only excitations in which the resultant state had total angular momentum J=3/2 were allowed, due to method VII being an attempt at improving convergence for the ${}^2D^o_{3/2}$ state.

8.2.4 Summary of all methods

In the table below the largest expansions of all methods described above are summarized. Note that direct comparison of expansions sizes across methods is not necessarily possible due to the expansions being generated with different active sets.

Table 8.4: Summary of all methods. Note that in all cases, restricted SD excitations include unrestricted SD excitations from $6sp$. Beware that the active sets vary from method to method, so direct comparison between active sets is not possible. Excitations with the aforementioned J=3/2 restriction again highlighted in bold.

Mthd.	From	Exc.	To	NCF
I	$6sp5spd4spdf3sp$	S	$4spdf$	6 865
II	$6sp5spd$	SD	$4spdfg1h$	768 994
III	$6sp$	SDT	$4spdf1gh$	771 194
IV	$6sp5spd4spdf3p$	SrD	$4spdfg1h$	714 496
V	$6sp5spd4spdf3sp$	S	$4spdfg1h$	83 725
	$6sp$	SD	$4spdfg1h$	
	$5spd6sp$	SD	$1spdfgh$	
VI	$6sp5spd4spdf3sp$	S	$4spdfg1h$	41 723
	$6sp$	SD	$4spdfg1h$	
	$6sp5spd$	SrD	$1spdfgh$	
VII	$6sp5spd4spdf3sp$	S	$4spdfg1h$	203 299
	$6sp5sp4spd$	SrD	$4spdfg1h$	
	6sp5sp4spd	**SrD**	**4spdfg1h**	
	$6sp5spd$	SrD	$1spdfgh$	
VIII	$6sp5sp4sp3sp2sp1s$	S	$4spdfg1h$	29 389
	$6sp$	SD	$4spdfg1h$	
	$6sp5sp$	SrD	$1spdfgh$	

8.3 The Breit-Rosenthal effect

The Breit-Rosenthal effect is quantified by calculating the dependence of A on the nuclear spatial distribution parameters mean squared charge radius and skin thickness. These were varied in two separate series of calculations, with mean squared charge radius varied for methods I, V, VI, and VIII, and skin thickness for methods VI and VIII. Both parameters were varied in the program RNUCLEUS, with their values defining the parameters of the Fermi distribution (3.1).

8.3.1 Mean squared charge radius

The mean squared charge radius was varied in increments of 0.25 fm^2 from $\langle r_0^2 \rangle - 1.5$ fm^2 to $\langle r_0^2 \rangle + 1.0$ fm^2. This range was selected based on an extension of the range tabulated by Angeli and Marinova [9]. Since their tabulated values encompass approximately $\langle r_0^2 \rangle \pm 0.4$ fm^2, with only bismuths $202-213$ included, the range used in this project was assumed to include most of the isotopic variation in mean squared charge radius for bismuth. The hyperfine constant was then calculated with these new charge radii, and simple linear regression was used to find the proportionality constant λ, such that $\delta A = \lambda \delta \langle r^2 \rangle$, δA here measured in percentages of the A calculated with $\langle r^2 \rangle = 5.5211(26)$ fm^2. This proportionality constant then served as a proxy value for the Breit-Rosenthal effect.

8.3.2 Skin thickness

Skin thickness was varied in in four steps, ± 0.1 fm, and ± 0.2 fm. Again, A was calculated for each skin thickness, and linear regression was used to determine the relation between variations in skin thickness and A. In the same manner as for mean squared charge radius, a linear fit was used to find the proportionality constant τ, such that $\delta A = \tau \delta t$, with δA this time being measured in percentages of the A calculated with $t = 2.3$ fm.

8.3.3 Linear regression

To quantify the Breit-Rosenthal effect, using the linear relationship of equation (6.18), a simple linear regression on the form $y = a + bx$ was used, with

$$a = \bar{y} - b\bar{x} \tag{8.1}$$

$$b = \frac{\sum_i (x_i - \bar{x})(y_i - \bar{y})}{\sum_i (x_i - \bar{x})^2} \tag{8.2}$$

Where, of course, $x = \delta \langle r^2 \rangle$, and $y = A$. The *coefficient of determination*, also known as R^2, was calculated using

$$R^2 = \frac{(\bar{xy} - \bar{x}\bar{y})}{(\bar{x^2} - \bar{x}^2)(\bar{y^2} - \bar{y}^2)} \tag{8.3}$$

This coefficient gives an indication on the quality of the linear fit, i.e. how justified the assumption of a linear correlation between the two variables are; the closer R^2 is to unity, the better the correlation.

8.4 Workflow optimization

In this project, a large number of calculations had to be done, both in the preliminary exploration of the active set, and in the actual calculation of the

target values. Due to this, good workflow was crucial, both to limit time usage, as well as to keep track of calculations.

8.4.1 Computational speed

As seen in the previous section, the number of configurations included in the calculation was typically in the tens to hundreds of thousands. Since the matrices of the equations to be solved grow with $(\mathrm{NCF})^2$, doing these calculations in a sequential fashion would quickly give unmanageable computational times. To avoid this, calculations were run using the Message Passing Interface (MPI) library OpenMPI [33], where possible. This allows for parallelization of the calculation, letting a single program run on several processor cores (or several CPUs), drastically cutting down time use. Somewhat counter-intuitively, the speed of calculation does not necessarily increase along with the number of processes used, and may in fact decrease in some cases. Some programs may be more difficult to parallelize, such as RMCDHF. A simple test of time use as a function of number of processes was run, once on a workstation used in the initial phase of the project, and once after moving the project over to Idun. Though most of the calculations used in the project were done on Idun, the results from the workstations are included to highlight the importance of actually considering each system, and not making assumptions based on calculations done on other computers. The optimal numbers of parallel tasks on the workstations were found to be two for RANGULAR_MPI[3] [4] and RMCDHF_MPI, and five or six for RCI_MPI. On Idun, however, the optimal number was found to be approximately 32 for RANGULAR_MPI and RMCDHF_MPI, and >48 for RCI_MPI.

[3] Note that almost all of the calculations done in this project were done with the NAME_MPI versions of the programs, even though the programs are referred to by their "main" name in the rest of the thesis.

[4] A quirk of GRASP is that RMCDHF_MPI reads from the same directory as RANGULAR_MPI writes to, and the file tree of that directory is dictated by the number of tasks. All of this to say that even though RANGULAR_MPI could benefit from having a higher number of tasks than RMCDHF_MPI, GRASP requires them to have use the same number of tasks. Since RMCDHF_MPI is the most computationally intense of these programs, it was prioritised over RANGULAR_MPI when deciding on the number of tasks.

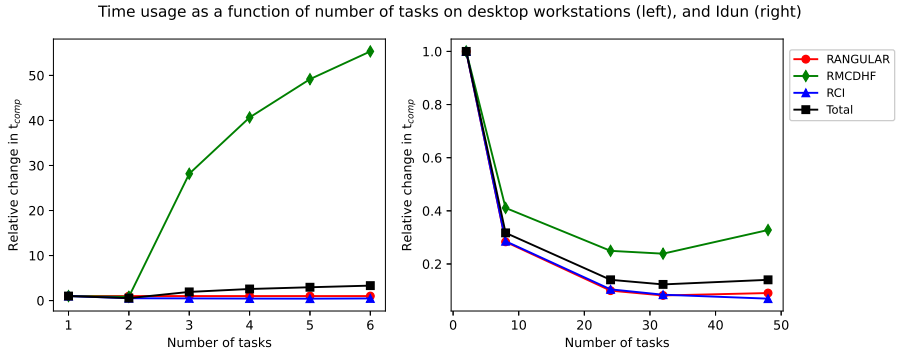

Figure 8.1: Relative increase in computational time as a function of number of MPI processes. The plot on the left shows the results for a desktop workstation used in the early phases of the project, and the one on the right shows the results for Idun.

Though it may be a bit difficult to see in (8.1), the vast increase in the time taken by RMCDHF, led to the total computational time being three times longer with six tasks than with one.

The discrepancy in optimal number of processes between the workstations and the cluster might be a result of the specifications of each, for instance a difference in read speed, or it might have to do with the general architecture of each system. Idun is specifically built for large calculations, after all.

Only the three MPI compatible programs, RANGULAR, RMCDHF, and RCI were tested. Increasing the number of compute nodes did not increase computational speed much when keeping the total number of processes constant. Whether the speedup was dependent on the size of the particular calculation was not considered, as only one configuration was tested. All subsequent calculations, run with these results in mind, were completed in so reasonable times as to not create the need for further optimization. Also, the main limiting factor in processor usage, was scheduling on the cluster. As more processor cores were requested, waiting times grew, and the program had to be restarted with a lower amount of cores to be able to run. Though a more thorough examination of the optimal settings could be of some use, the main purpose of this test was to get a rough idea of how to run the calculations without experiencing the kind of slowdown seen in figure 8.1.

8.4.2 Scripts

The amount of input required by each of the programs used in this project varies a lot, from one line in RANGULAR, to 19 in RMCDHF. Inputting these parameters by hand is a tedious task, especially when doing calculations on a large number of subshells. Giving the inputs manually also increases the risk of human errors. Luckily, the input to the GRASP programs varies little from

run to run, allowing new calculations to be initiated with just a few new lines of input. Using simple bash[5] scripts to pass arguments to the programs, the input process was vastly simplified.

The basic script structures were similar to those described in chapter 10 of the user manual [21, pp. 213-228]. The programs RCSFGENERATE, RCSFINTERACT, and RWFNESTIMATE were all gathered in a single script, init, and all subsequent program calls were done in separate scripts. This structure made for easy repetition of singular steps in the calculation, allowing for better control.

Handling errors

In GRASP, there are a few key ways a calculation may end without completing. The easiest to deal with are the fatal errors; if the program encounters erroneous inputs, or missing files, it might end with some error message describing the problem. Since these end the calculation, they are hard to miss, and can often be fixed by redoing the calculations from an earlier step, or by proofreading the scripts. The ones that are harder to handle, are the non-fatal errors, where the program encounters a problem, but powers through it. One such non-fatal error that was frequently encountered in the later calculations run on Idun, had to do with a faulty call to some of the MPI protocols. The error message warns that the program may act unpredictably and/or abort, though these effects were never observed, the program was restarted as many times as needed for it to run without error. Another "error" occurs if the self-consistent calculation exceeds the maximum number of iterations allotted to it[6]. To handle non-fatal errors on Idun, a simple script was used that read through the output files, and returned the line containing one of the errors included in the script. It was mostly used to avoid the aforementioned MPI error, but was also used to check for convergence in the self-consistent calculation, as well as anything output as "error".

8.4.3 Changing the default parameters of the package

In an attempt to solve a problem with the scripts [7], the values for RNT and H in the source code were rewritten. This was done using the standard bash commands "sed" and "grep", with care taken not to change unrelated variables. These changes did not seem to adversely affect the program's ability to run, and the results matched well with results attained without these edits, both from previous and subsequent runs. The main difference seemed to be the changing of the default accuracy of RMCDHF, which increased the time needed to run that program by up to several times the "unedited" time. The accuracy of

[5] For the uninitiated: bash is short for Bourne-Again SHell, and is the command language used in the terminal of most Linux distributions.

[6] Though this is not an error, it may impact the accuracy of the calculations if the maximum number of iterations is set too low. This did not happen in the present work, though there were instances of the calculation exceeding the maximum number of iterations due to the program running in a loop.

[7] The problem turned out to be a non-issue, a result of lacking experience with bash scripts.

the RMCDHF program is defined by $ACCY = H^6$ [34], which fits well with the observed behaviour of the program. Considering that the default accuracy when determining convergence in RMCDHF is on the order of 10^{-8}, the increase in precision was deemed too small to make up for the increase in computational time. It is worth noting that the default grid parameters and accuracy can easily be changed by answering "n" (no) to any prompt asking if default parameters are to be used [34]. The results found in this report were all acquired on computers with the standard (source code) values for RNT and H, with grid parameters updated as part of the program inputs. The only edits to the source code were in expanding the number of radial grid points from the default N=590, to N=2990, which was done according to the manual [21, pp. 20-21].

Chapter 9

Results

In what follows, the results of the three main calculations of this project, converging A towards experimental values, determining the proportionality constant λ such that $\delta A = \lambda \delta \langle r^2 \rangle$, and determining the proportionality constant τ such that $\delta A = \tau \delta t$, will be given for each method.

9.1 Convergence of A

Attempts at achieving convergence towards the experimentally measured values of A from [25] were made for all methods. The results will be given in a "quantitative" fashion, highlighting which subshells were included at each step, rather than the total size of the active set. This has the added benefit of making comparisons between different virtual sets easier. Tables containing the total active spaces can be found in appendix C.

9.1.1 Method I

With only single excitations allowed, two of the five states converged to within $\pm 5\%$ of the experimentally measured values. Of the other three, none came closer than 22%, though the calculations converged fairly well towards the wrong values.

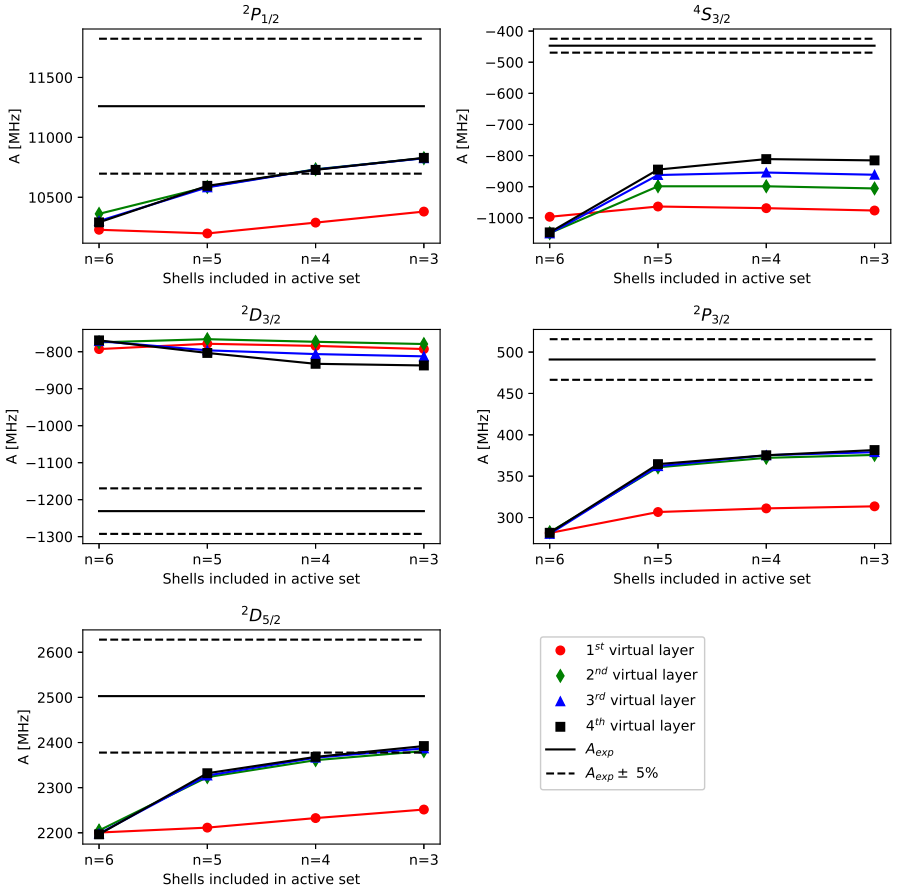

Figure 9.1: Convergence towards experimentally measured A for all five states using method I.

As the figure shows, most of the effects on A came from the expansion of the spectroscopic set, as expanding the virtual set had little effect after the second virtual layer was added. The largest expansion with this method yielded 6 895 CSFs.

9.1.2 Method II

With method II, using unrestricted SD excitations, the expansion sizes quickly grew unmanageable, so only one additional expansion of the spectroscopic set was included.

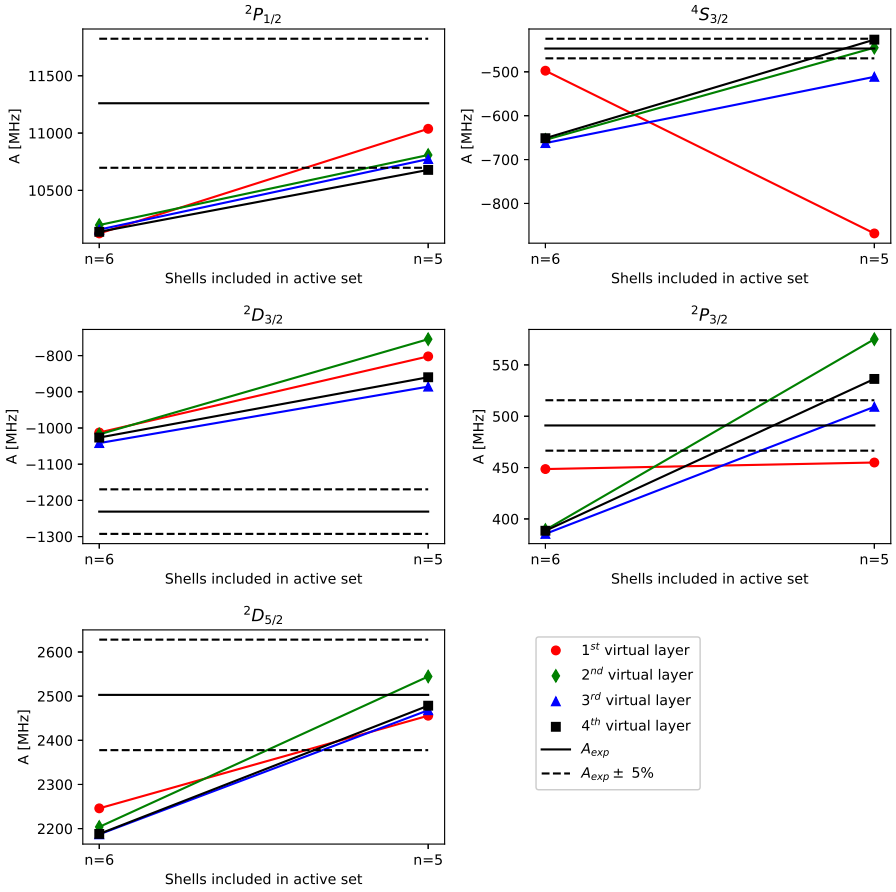

Figure 9.2: Convergence towards experimentally measured A for all five states using method II.

The plots indicate that the convergence achieved with this method does not make up for the computational cost, considering that the largest expansion gave 768 994 CSFs. The relatively large difference between the calculation done with three virtual layers and the one with four also shows that at least five virtual layers should be included when using unrestricted SD excitations only.

9.1.3 Method III

With unrestricted SDT excitations, the number of CSFs exceeded 700 000 already at n=6, so no further expansions were made.

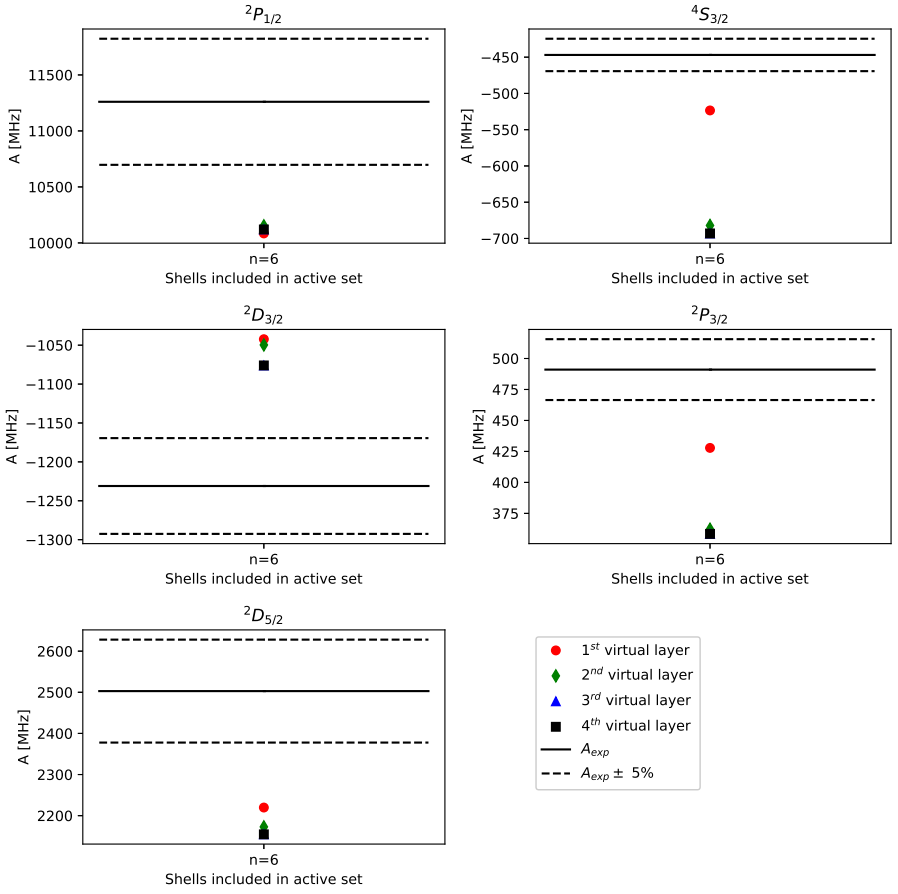

Figure 9.3: Convergence towards experimentally measured A for all five states using method III.

Though the plots above are a bit hard to read, only having one data point per virtual layer, they show that unrestricted SDT excitations do not give good convergence, compared to the number of configurations, which for the fourth virtual layer was 771 194.

9.1.4 Method IV

With restricted SD excitations, a higher number of spectroscopic orbitals could be included for a comparable number of configurations as the unrestricted methods.

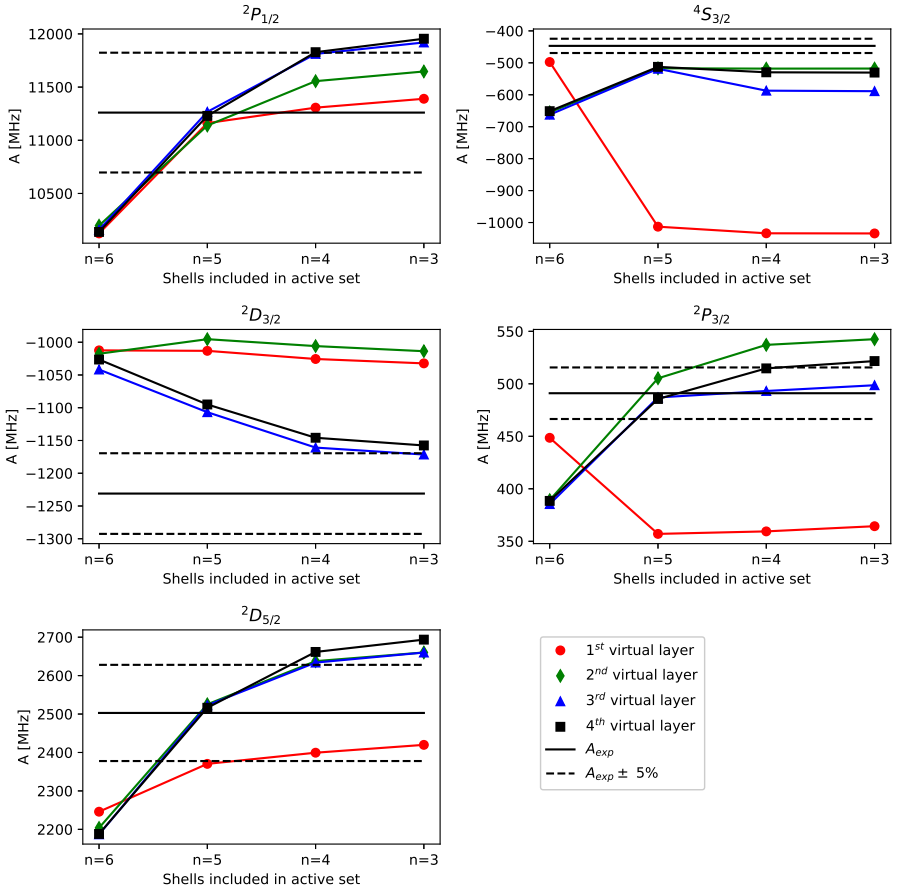

Figure 9.4: Convergence towards experimentally measured A for all five states using method IV.

The convergence is markedly improved from the previous three methods, however the largest expansion still generated 714 496 CSFs, thus coming at a high computational cost. There is also the same problem as for method II, namely that the convergences indicate the need for a fifth virtual layer.

9.1.5 Method V

The first of the Bieroń-Pyykkö methods, which used S excitations augmented by unrestricted SD excitations.

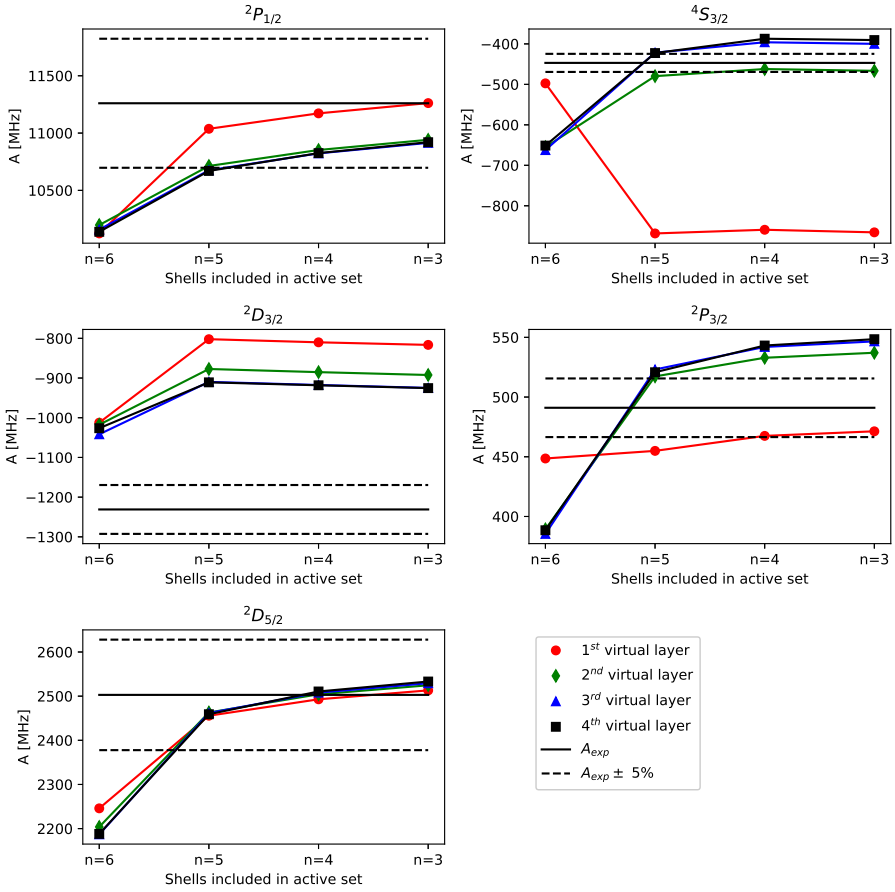

Figure 9.5: Convergence towards experimentally measured A for all five states using method V.

As the plots show, fair convergence was achieved in three of the five states. At NCF = 83 725, the method also generated far fewer CSFs than the three previous methods. The relative change when going from three to four virtual layers was small enough that expanding the virtual space further was not necessary.

9.1.6 Method VI

When imposing restrictions on the SD excitations from the previous method, the following convergences were achieved:

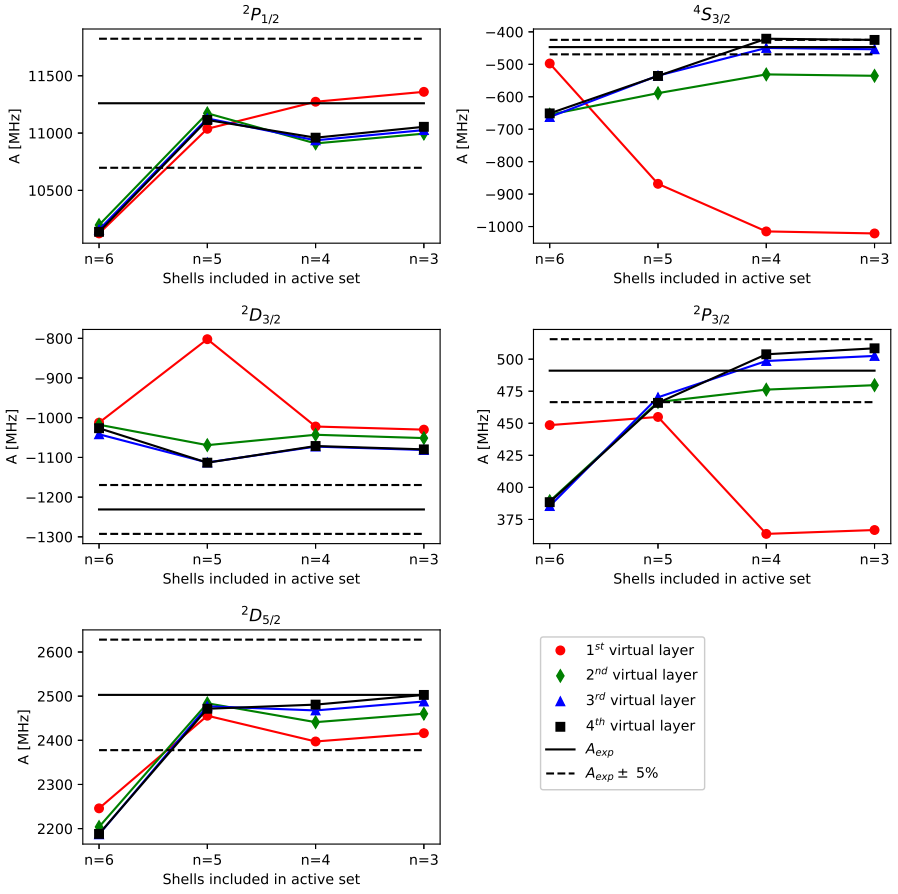

Figure 9.6: Convergence towards experimentally measured A for all five states using method VI.

With restrictions, four out of the five states converged satisfactorily, at approximately half the number of "unrestricted" CSFs: 41 723. In the same manner as for method V, there was no need for a fifth virtual layer. There is a possibility that further expanding the spectroscopic set, including some n=2 subshells, could have benefited the project, but the convergence was good enough that this was not deemed necessary.

9.1.7 Method VII

This method expanded on the restricted Bieroń-Pyykkö method by adding an extra set of restricted SD excitations in the J=3/2 states. Note that in the plots below, the extra calculations with this method are appended to the plots of the previous method, marked with "VII". Only the maximal expansion, with n=3,

was included. The results for n=6,5,4,3 are the same as in figure 9.6.

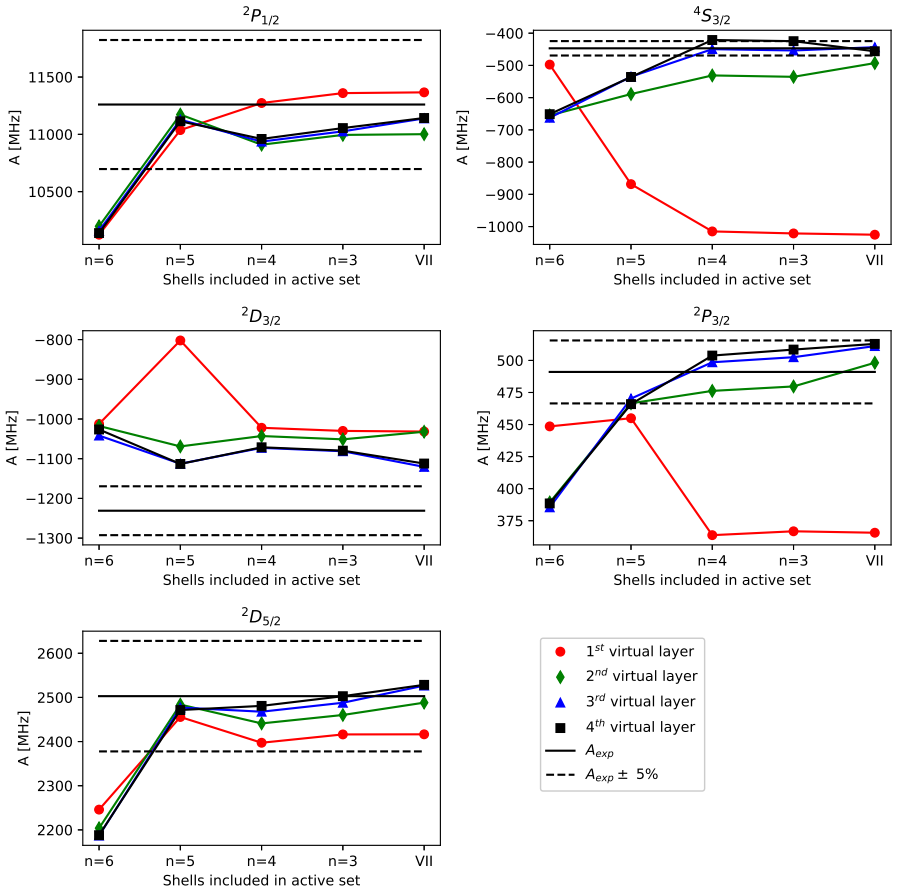

Figure 9.7: Convergence towards experimentally measured A for all five states using method VII.

Compared to the previous method, there is an improvement in the convergence of most states. The largest expansion of this method generated 203 299 CSFs, almost five times the amount of method VI.

9.1.8 Method VIII

This last method implemented the restricted Bieroń-Pyykkö method (VI), but with only $l = s, p$ subshells included in the spectroscopic set.

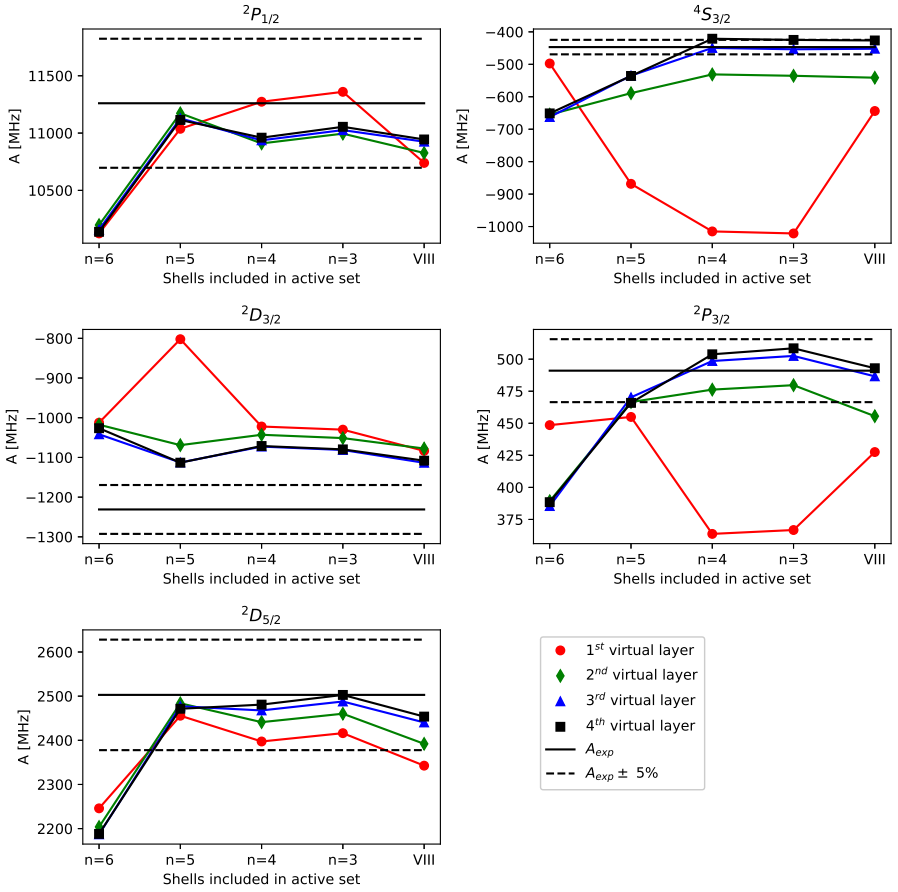

Figure 9.8: Convergence towards experimentally measured A for all five states using method VIII.

As for the previous method, only the largest expansion, with n=3, of this method was included in the calculations. The results are marked "VIII" in the figure above. The convergence is clearly comparable to the previous two methods, but at the second-to-lowest number of CSFs of all methods: 29 389.

9.2 Variation in mean squared charge radius

Based on the convergences in the section above, four methods were selected for variations in nuclear mean squared charge radius, those being methods I, VI, VII, and VIII. For each of these methods, a linear fit $\delta A = \lambda \delta \langle r^2 \rangle$ was made. In the figure below, these linear fits will be shown, overlapped to highlight agreement across methods.

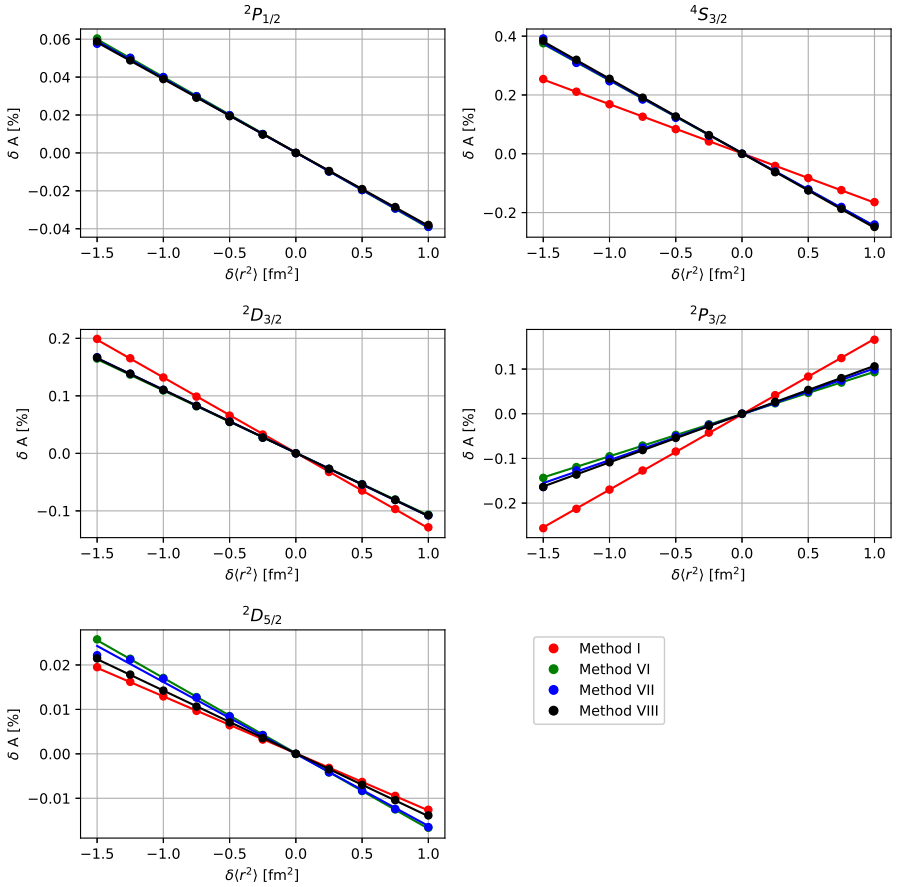

Figure 9.9: Linear fit of the relation $\delta A = \lambda \delta \langle r^2 \rangle$ for methods I, VI, VII, and VIII.

The table below contains the proportionality constants λ and coefficients of determination, R^2 attained from the linear fits in the figure above, as well as the discrepancy between calculated and experimentally measured A, in percentages of the latter.

Table 9.1: Summary of all the methods for which λ were calculated. The units are [%fm^{-2}] for λ, and [%] for ΔA.

Mthd.	Var.	$^2P^o_{1/2}$	$^4S^o_{3/2}$	$^2D^o_{3/2}$	$^2P^o_{3/2}$	$^2D^o_{5/2}$
I	λ	-0.039	-0.167	-0.131	0.169	-0.013
	R^2	>0.999	>0.999	>0.999	>0.999	>0.999
	ΔA	3.83	82.44	32.0	22.29	4.42
VI	λ	-0.040	-0.248	-0.109	0.095	-0.017
	R^2	>0.999	>0.999	>0.999	>0.999	>0.999
	ΔA	1.83	4.96	12.29	3.55	0.00
VII	λ	-0.039	-0.249	-0.110	0.103	-0.016
	R^2	>0.999	>0.999	>0.999	0.998	0.996
	ΔA	1.04	2.06	9.65	4.45	1.02
VIII	λ	-0.039	-0.253	-0.110	0.108	-0.014
	R^2	>0.999	>0.999	>0.999	>0.999	>0.999
	ΔA	2.81	4.58	9.98	0.39	1.96

9.3 Variation in skin thickness

Only two methods were selected for variations in skin thickness, VI and VIII, due this effect being assumed to be less important than variations in mean squared charge radius. As will be shown below, this assumption was correct, and further exploration of the relationship between A and t was not pursued.

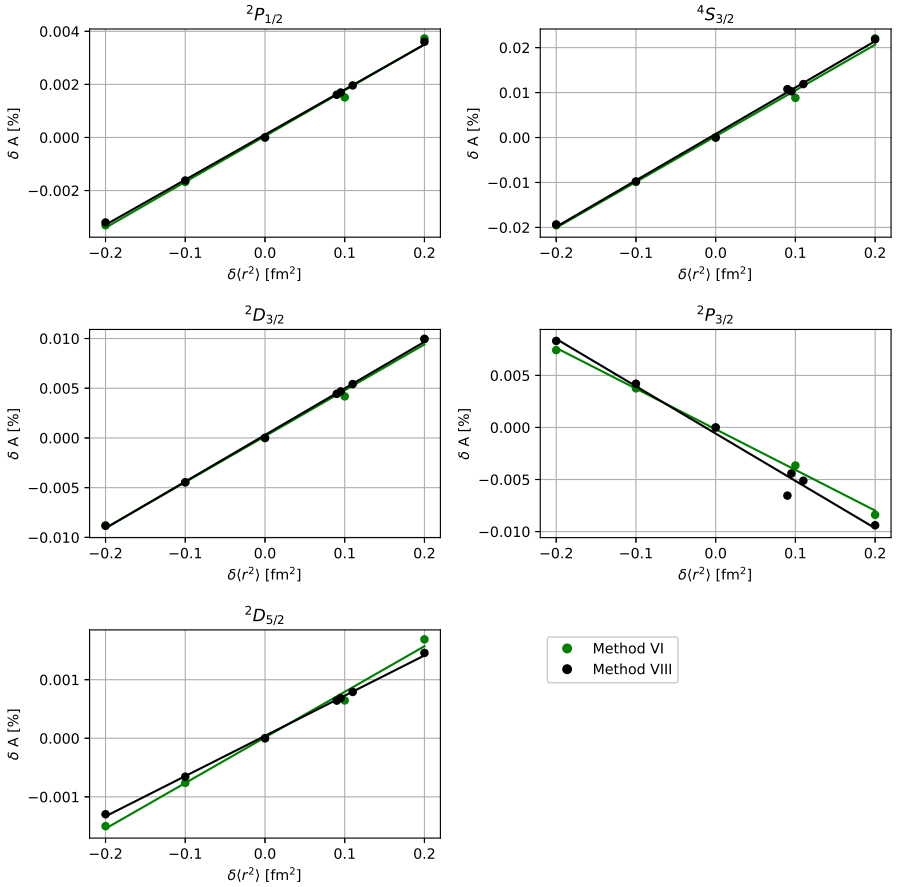

Figure 9.10: Linear fit of the relation $\delta A = \tau \delta t$ for methods VI and VIII.

When varying the skin thickness using the expansions of method VIII, some strange results appeared. With $\delta t = 0.1fm$, values of δA several times higher or lower than for the neighbouring points were calculated. These were assumed to be random artefacts of the computation, and additional calculations were done with $\delta t = 0.9, 0.95, 0.11$, to rule out any actual, physical effects at this skin thickness. Except for a single point in the plot for $^2P^o_{3/2}$, the figure shows that these additional calculations indicate that the strange values were erroneous, as first believed. A plot including the aberrant values can be found in appendix B.

The table below summarizes the results for variations in skin thickness.

Table 9.2: Summary of all the methods for which τ were calculated. The units are [%fm^{-1}] for τ, and [%] for ΔA.

Mthd.	Var.	$^2P^o_{1/2}$	$^4S^o_{3/2}$	$^2D^o_{3/2}$	$^2P^o_{3/2}$	$^2D^o_{5/2}$
VI	τ	0.017	0.102	0.046	-0.039	0.008
	R^2	0.996	0.995	0.996	0.997	0.994
	ΔA	1.83	4.96	12.29	3.55	0.00
VIII	τ	0.017	0.103	0.047	-0.045	0.007
	R^2	>0.999	0.999	0.999	0.981	>0.999
	ΔA	2.81	4.58	9.98	0.39	1.96

Chapter 10

Discussion

10.1 On the results

Akin to previous results acquired for the similarly heavy isotopes ^{199}Hg [35] and ^{207}Pb [36], the majority of the Breit-Rosenthal effect was found to originate from the change in the nuclear mean squared charge radius, with the effect of variations in skin thickness generally being an order of magnitude or more lower than that of the charge radius.

10.1.1 Convergence of A

As figures 9.1-9.8 show, the convergence of the calculated magnetic dipole hyperfine constants to the experimentally measured ones varied a lot between methods. As mentioned in chapters 8 and 9, four of the eight methods gave poor convergence compared to computational cost, and were not included for calculations on the Breit-Rosenthal effect. Three of the methods (II, III, IV) generated more than 700 000 CSFs, which even on an hpc cluster like Idun requires many hours of computational time. The unrestricted SDT excitations of method III had the poorest performance, due to only one spectroscopic subshell being feasible to include. The Bieroń-Pyykkö methods, especially the restricted ones, generally gave good convergence compared to computational cost, and can be recommended as a starting point for explorations of similarly large systems in future research.

The benchmark of acceptable convergence in this project, was whether the calculated hyperfine constant got to within ±5% of the experimentally measured values tabulated by Wilman, Ruczkowski, and Elantkowska [25]. In the table below, the quantity $\sqrt{\sum |\Delta A|^2}$, with $\Delta A = A_{exp} - A_{calc}$ is used as a measure of convergence, reported for the largest expansion for each of the methods described above. The maxima and minima of ΔA for each method are also listed.

Table 10.1: Summary of the different methods, with the quantity $\sqrt{\sum |A_{exp} - A_{calc}|^2} = \sqrt{\sum |\Delta A|^2}$ used as an indicator for the convergence towards the experimentally measured values of the hyperfine constant, along with the highest and lowest ΔA for each method.

Mthd.	NCF	$\sqrt{\sum \lvert\Delta A\rvert^2}$	$(\Delta A)_{min}$	$(\Delta A)_{max}$
I	6 865	91.39	3.83	82.44
II	768 994	32.3	0.98	30.16
III	771 194	22.82	5.97	18.71
IV	714 496	64.93	10.12	55.07
V	83 725	30.39	1.21	24.83
VI	41 723	13.84	0.00	12.29
VII	203 299	10.92	1.02	9.65
VIII	29 389	11.51	0.39	9.98

As the table shows, a higher number of configuration states does not necessarily imply more accurate results. Due to poor convergence vis-à-vis number of CSFs, methods II, III, IV, and V were not used in the calculations on the Breit-Rosenthal effect, as mentioned earlier. Method I was included, despite its generally poor convergence, due to its low computational cost. It also showed good convergence for the two J=1/2, 5/2 states, allowing it to be used as a simple test of whether calculated values of λ were dependent on expansion method, and not just convergence to A_{exp}.

On the state $^2D^o_{3/2}$

As is clear from figures 9.1-9.8, the state $^2D^o_{3/2}$ was exceedingly difficult to achieve convergence for. The closest approach was with method IV, the restricted SD excitations. With that method, the calculated A($^2D^o_{3/2}$) got to within about 6% of the experimentally measured value, though at too great a computational cost to be useful in estimating the Breit-Rosenthal effect. Method VII was an attempt at combining methods IV and VI, thus, hopefully, attaining good convergence for $^2D^o_{3/2}$ while not creating infeasible calculations. The attempt worked somewhat, as this method gave better convergence for the state than the previous method, however similar convergence at a far lower computational cost was attained in method VIII. While further exploration of the expansion methods could be useful, it was decided to prioritize the other states, especially the ground state $^4S^o_{3/2}$.

10.1.2 Variation in mean squared charge radius

As can be seen from table 9.1, the calculated values of λ are quite independent of the chosen method, depending more strongly on the value of ΔA. Considering method VIII in light of this observation, we see that even though s and $p_{1/2}$

orbitals are the orbitals that contribute to the Breit-Rosenthal effect, deep-core orbitals are not necessary to estimate its size. However, the acquired accuracies were comparable to the other methods, but required fewer configurations, meaning that only including $l = s, p$ orbitals might be a valid approach to calculating the Breit-Rosenthal effect.

By only including λ's for which $\Delta A < 5\%$ (thus excluding ${}^2D^o_{3/2}$ in its entirety) we see that λ falls within the following intervals for the four remaining states

$$
\begin{aligned}
{}^2P^0_{1/2} &: \lambda \in (-0.040, -0.039) && \Rightarrow \Delta\lambda = 0.001 = 2.56\% \\
{}^4S^0_{3/2} &: \lambda \in (-0.253, -0.248) && \Rightarrow \Delta\lambda = 0.005 = 2.01\% \\
{}^2P^o_{3/2} &: \lambda \in (0.095, 0.108) && \Rightarrow \Delta\lambda = 0.013 = 12.04\% \\
{}^2D^o_{5/2} &: \lambda \in (-0.017, -0.013) && \Rightarrow \Delta\lambda = 0.004 = 23.53\%
\end{aligned}
$$

Where the rightmost values give the length of the interval as a percentage of the λ calculated with the smallest ΔA. Somewhat surprisingly, there seems to be little correlation between accuracy of estimated A, and length of the intervals, indicating that the different states may have differing sensitivities to variations in $\langle r^2 \rangle$. The best accuracies (lowest ΔA's) were in fact attained for the ${}^2D^o_{5/2}$, the state with the highest percentage-wise uncertainty in λ. Now, it is worth mentioning that even though the percentage-wise errors do vary, the absolute errors are quite stable. Except for in the case of ${}^2P^o_{3/2}$, all errors are in the third decimal, which indicates that the method used to calculate the values has high reliability.

Based on the values above, as well as those in table 9.1, the recommended values for the four most precisely calculated states are given in the table below. The uncertainties are set at twice the interval spanned by the calculated values of λ. For comparison, the results acquired by Heggset and Persson for Hg [35], and Karlsen and Persson for Pb [36] are included.

Table 10.2: Recommended values for the proportionality constants λ, as calculated in the present work. Previously calculated results for Hg and Pb are included for comparison.

	State	λ [%fm^{-2}]	Source
Bi I	$6p^3\ ^2P^o_{1/2}$	-0.039(2)	
	$6p^3\ ^4S^o_{3/2}$	-0.249(10)	
	$6p^3\ ^2D^o_{3/2}$	$\approx$ -0.1	
	$6p^3\ ^2P^o_{3/2}$	0.105(26)	
	$6p^3\ ^2D^o_{5/2}$	-0.017(8)	
Hg I	$6s6p\ ^3P_1$	-0.11(1)	[35]
	$6s6p\ ^3P_2$	-0.12(1)	[35]
Pb I	$6p^2\ ^3P_1$	-0.083(2)	[36]
	$6p7s\ ^3P_1$	-0.065(3)	[36]
	$6p^2\ ^3P_2$	-0.009(4)	[36]
	$6p^2\ ^1D_2$	0.09(2)	[36]

When comparing the results in this project with the values calculated for Hg and Pb, we can see that all values fall within the same two orders of magnitude, indicating that the values calculated in the present work are reasonable.

On $\lambda(^2D^o_{3/2})$

As the table above shows, it was chosen to only give a rough estimate of the proportionality constant $\lambda(^2D^o_{3/2})$. The results shown in figure 9.9 indicate that this value lies in the vicinity of 0.1, probably closer to 0.11, due to the consistency of the three lines corresponding to methods VI, VII, and VIII, but since the calculated values of A did not meet the set criteria for convergence, it was chosen to take the safe approach, and only give an approximate value.

10.1.3 Variation in skin thickness

As the last plot in chapter 9 (figure 9.10), as well as table 9.2, show, variations in skin thickness have little impact on the calculated hyperfine constant A. Even by extending the range of possible skin thicknesses to $t \in [2.0, 3.0]$ fm, which exceeds that found in the literature, the values of A across that interval would differ by, at most, approximately 0.1%, based on the calculated values of τ. This validates the approach used in this project, wherein the value $t = 2.3$ fm is used as the standard skin thickness for heavier isotopes, as posited in the "Handbook of Relativistic Quantum Chemistry" [15, p. 57]. Based on this, as well as the previous results for Hg and Pb [35, 36], it does not seem vital to have precision measurements of the skin thickness in order to get good estimates of the Breit-Rosenthal effect.

10.1.4 Comparison with hyperfine anomalies

Little effort has been made in measuring the hyperfine anomalies of bismuth, and even less for the non-ground states, so the comparisons to literature will only deal with the ${}^4S^o_{3/2}$ state. Thanks to Billowes and Campbell [37] combining their own laser spectroscopy measurements, with previously acquired results for the hyperfine constants and magnetic dipole moments of most bismuth isotopes with $A \in [202, 213]$, there is ample opportunity to compare the predicted values of the Breit-Rosenthal effect in the present work, with calculated hyperfine anomalies along the isotopic chain. Sadly, the results reported by Billowes and Campbell carry with them quite significant uncertainties, so the results will be discussed in terms of intervals gotten by calculating the maximal and minimal values of the hyperfine anomaly, with the given uncertainties. The values for ^{209}Bi will be the ones given in table 3.1.

Table 10.3: Calculated hyperfine anomalies based on previously measured values of A(${}^4S^o_{3/2}$) and μ. Values are taken from [37] unless otherwise specified.

A(I^π)	A [MHz]	μ [μ_N]	${}^A\Delta^{209}_{min}$ [%]	${}^A\Delta^{209}_{max}$ [%]	$\lambda\delta\langle r^2\rangle_{A,209}$
202 (5^+)	-405(10)	4.259 (14)	1.25	5.29	0.102(5)
202 (6^+)	-343(7)	4.325(13)	1.55	4.83	0.102(5)
203 ($\frac{9}{2}^-$)	-433(6)	4.017(13)	0.313	2.31	0.0822(38)
204 (6^+)	-433(6)	4.322(15)	-2.41	14.9	0.0760(38)
205 ($\frac{9}{2}^-$)	-437.0(10)	4.065(7)	1.566	1.582	0.0558(25)
206 (6^+)	-356.1(15)	4.361(8)	0.1307	0.5077	0.0488(22)
207 ($\frac{9}{2}^-$)	-443.99(24)	4.0915(9)	0.63077	0.66375	0.0296(17)
208 (5^+)	-462(5)	4.633(10)	-0.612	-2.27	0.0177(12)
208 (5^+) [38]	-446.05(32)	4.570(10)	0.51329	0.90198	0.0177(12)
210 (1^-)	21.78(3)	-0.04451(6)	0.3904	0.4932	-0.0247(17)
210^m (9^-)	-147(6)	2.728(42)	-1.09	3.83	-0.0247(17)
213 ($\frac{9}{2}^-$)	-399.3(18)	3.716(7)	1.409	1.830	-0.104(4)

Clearly, from the table, the absolute magnitude of the calculated Breit-Rosenthal effect is significantly smaller than the hyperfine anomaly intervals suggested by Billowes and Campbell[1]. Though the values are too spread to make any precise inferences on their actual relative importances. It is also interesting to note that for the values of ^{205}Bi and ^{206}Bi, measured to similar precision, the table indicates that the Breit-Rosenthal effect is a larger contributor to the hyperfine anomaly in the case of the even-numbered isotope, than the odd-numbered one. One would expect that the Breit-Rosenthal effect is, rel-

[1]Except for in the cases of ^{204}Bi and ${}^{210^m}$Bi, where the intervals span both positive and negative values. This is of little importance, however, due to the large uncertainties in the measurements.

atively speaking, largest for the odd-A isotopes, as their identical nuclear spins makes for smaller variation in magnetization, and thus a smaller contribution from the Bohr-Weisskopf effect. When comparing the results for the hyperfine anomaly $^{208}\Delta^{209}$ calculated with the values from Billowes and Campbell [37] and the ones from Schmidt et al. [38], we see that it is difficult to directly compare the calculated values, with measurements from the literature as the experimental values may differ greatly. High-precision measurements of the hyperfine anomalies along the bismuth isotopic chain are necessary before such comparisons can be made.

10.2 On the methods used

10.2.1 On the linear correlation between A, and $\delta\langle r^2\rangle$, and A and δt

As is easily seen from the plots in chapter 9 (9.9-9.10), the assumption of a linear correlation between the magnetic dipole hyperfine constant and the nuclear mean squared radius and skin thickness seems justified. Looking at the coefficients of determination, most of the linear fits have $R^2 > 0.99$, indicating very good fits. The outlier here being the results for variations in skin thickness for the state $^2P^o_{3/2}$, due to the aberrant values around $\delta t = 0.1$ fm.

10.2.2 On the active set approach

The expansions and accuracies reported in the present project highlight both the importance of systematically exploring the active set with different expansion methods, and of adapting the workflow to the computer architecture on which the calculations are to be performed. There is a large difference, in terms of computational time, between doing non-optimized calculations on active sets in excess of 700 000 expansions on a desktop workstation, and doing calculations on a few tens of thousand configurations on a hpc cluster. The computational time might, in fact, be the difference between a project doable within a few days or weeks, and one that is not feasible in the slightest. For future calculations on large atomic systems, it can be recommended to consider the restricted Bieroń-Pyykkö methods, as they showcase the possibility of combining high accuracy with low computational cost.

Simultaneous optimization of all states

Though several methods were tested, none gave simultaneous convergence to within ±5% for all five states considering in this thesis. At best, four out of the five states converged to a satisfactory degree, while the fifth, without exception being $^2D^o_{3/2}$, got to within about ±10%. Method III, using SrD excitations got this troublesome state to within ±6%, though at the cost of generating more than 700 000 configurations. Though further exploration may have led to a

"silver bullet" expansion for ^{209}Bi, it was decided to leave well enough alone. As table 9.1 shows, the calculated values of λ did not necessarily depend heavily on the accuracy of the corrected A, with calculated values being of the same order of magnitude even when the absolute value of $\Delta A = A_{exp} - A_{calc}$ were in excess of 80 percentage points. The table also highlights the fact that simply throwing more configurations at a problem does not necessarily lead to a higher accuracy. Comparing ΔA and NCF for the J=3/2 states using method VII and method VIII, we see that at more than ten times the number of configurations, method VII did not markedly improve convergence towards A_{exp}, in one case even giving a less accurate result. This shows that a more selective approach towards generating expansions is well preferable to the brute force approach.

Partitioning of the list of CSFs (rcsfzerofirst)

Chapter 14 of the GRASP user manual [21, pp. 299-318] is dedicated to managing large expansions by separating the CSFs into zeroth- and first-order spaces, based on the relative importance of the CSFs in building the ASF. Neither the manual nor the accompanying theoretical paper [18] give a threshold for when this method should be employed, only that it is useful when the "CSF expansions get so large that the cannot be handled by the normal SCF procedure" [21, p. 299]. By the use of the Bieroń-Pyykkö methods in this project, the expansion sizes were of such a scale that the calculations were easily done within minutes to hours on Idun. Were this not the case, for instance, if the SD or SDT expansions gave far superior results, this partitioning may have been employed in the calculations, but as it stands, the need never arose. Future studies seeking to either improve upon the results, or in similar calculations on other elements, in which the active set are further expanded, may benefit from this method.

10.2.3 Selection of states

In this project, only the $6p^3$ states of bismuth were examined. Of interest, due to its frequent appearances in the literature, would be the state $6p^2 7s^1\ ^4P_{1/2}$, which is responsible for the well-studied 3067-Å line [39–41]. Though this was considered, convergence issues made it difficult to work with. Even attempting to do calculations with only the three $J = 1/2$ even parity states, gave convergence issues not salvageable by changing Z, nor by gradually building up the core, as described in chapter 13 of the manual [21, pp. 271-298]. Calculations on this state were not pursued further, and quantifying the Breit-Rosenthal effect for the most important even-parity states is left for future study.

Chapter 11

Conclusion

In this thesis, the size of the Breit-Rosenthal effect for the $6p^3$ states of bismuth ($^2P^o_{1/2}$, $^4S^o_{3/2}$, $^2D^o_{3/2}$, $^2P^o_{3/2}$, and $^2D^o_{5/2}$) was studied using a multiconfigurational Dirac-Hartree-Fock calculation with relativistic and QED corrections applied in a configuration interaction calculation (MCDHF-CI), using the general-purpose relativistic atomic structure package GRASP2018. The Breit-Rosenthal effect was quantified as $\Delta_{BR} = \lambda\delta\langle r^2\rangle$, where $\langle r^2\rangle$ is the mean squared charge radius of the nucleus, and λ is a proportionality constant describing how the magnetic dipole hyperfine constant A changes with variations in mean squared charge radius. The Breit-Rosenthal corrections for the five states were found to be $\lambda(6p^3\ ^2P^o_{1/2}) = -0.039(2)$, $\lambda(6p^3\ ^4S^o_{3/2}) = 0.249(10)$, $\lambda(6p^3\ ^2D^o_{3/2}) \approx -0.1$, $\lambda(6p^3\ ^2P^o_{3/2}) = 0.105(26)$, $\lambda(6p^3\ ^2D^o_{5/2}) = -0.017(8)$, the orders of magnitude of which line up with previous calculations done on Hg [35] and Pb [36]. It was found that variations in nuclear skin thickness had little impact on the calculated Breit-Rosenthal corrections, the effect of which was therefore neglected in the reported results, also indicating that a "standard" skin thickness of 2.3 fm can be implemented in similar calculations. Further, the connection between expansion size and accuracy in the active set approach was examined, finding that rather than increase the size of the calculations, strategic and systematic explorations of the active set yielded the best result for the lowest computational cost. With the methods described in this project, calculations on heavy atoms, such as bismuth, may even be achievable on consumer-grade personal computers, eliminating the need for large, and expensive mainframes.

11.1 Future study

Further optimization of the expansions in this project, specifically with the aim of improving convergence for the $^2D^o_{3/2}$ state, and expanding the multireference, could serve to strengthen the reliability of the results reported in this thesis.

Solving the convergence issues with the even-parity states, especially the important $^4P_{1/2}$ state could give further insight into the composition of the

hyperfine anomaly in the bismuth isotopes.

Lastly, improving the experimental results for the hyperfine anomalies in the bismuth isotopes, would open the results of the present work up for further application in estimating the relative importance of the Breit-Rosenthal effect on the anomalies along the isotopic chain. As it stands, the uncertainties in the available data are too severe for such comparison.

References

1. Barzakh, A. E. *et al.* Hyperfine anomaly in gold and magnetic moments of $I^{\pi} = 11/2^{-}$ gold isomers. *Phys. Rev. C* **101,** 034308. https://link.aps.org/doi/10.1103/PhysRevC.101.034308 (3 Mar. 2020).
2. Stone, N., Stuchbery, A. & Dimitriou, P. *Evaluation of Nuclear Moments* tech. rep. (International Atomic Energy Agency, 2017).
3. Cowan, R. D. *The Theory of Atomic Structure and Spectra* (University of California Press, 1981).
4. Condon, E. U. & Shortley, G. H. *The Theory of Atomic Spectra* (Cambridge University Press, 1935).
5. Pais, A. *Inward Bound - Of Matter and Forces in the Physical World* (Oxford University Press, 1986).
6. Eisberg, R. & Resnick, R. *Quantum Physics of Atoms, Molecules, Solids, Nuclei, and Particles* 2nd ed. (John Wiley & Sons, 1985).
7. Rudzikas, Z. B. *Theoretical atomic spectroscopy* (Cambridge University Press, 1997).
8. Sitenko, A. & Tartakovskii, V. *Theory of Nucleus - Nuclear Structure and Nuclear Interaction* (Kluwer Academic Publishers, 1997).
9. Angeli, I. & Marinova, K. Table of experimental nuclear ground state charge radii: An update. *Atomic Data and Nuclear Data Tables* **99,** 69–95. ISSN: 0092-640X. https://www.sciencedirect.com/science/article/pii/S0092640X12000265 (2013).
10. Huang, W., Wang, M., Kondev, F., Audi, G. & Naimi, S. The AME 2020 atomic mass evaluation (I). Evaluation of input data, and adjustment procedures*. *Chinese Physics C* **45** (Mar. 2021).
11. Stone, N. J. *Table of recommended nuclear magnetic dipole moments* tech. rep. (International Atomic Energy Agency, 2019).
12. Stone, N. Table of nuclear electric quadrupole moments. *Atomic Data and Nuclear Data Tables* **111-112,** 1–28. ISSN: 0092-640X. https://www.sciencedirect.com/science/article/pii/S0092640X16000024 (2016).
13. Elton, L. R. B. *Nuclear Sizes* (Oxford University Press, 1961).

14. De Vries, H., De Jager, C. & De Vries, C. Nuclear charge-density-distribution parameters from elastic electron scattering. *Atomic Data and Nuclear Data Tables* **36,** 495–536. ISSN: 0092-640X. https://www.sciencedirect.com/science/article/pii/0092640X87900131 (1987).

15. Andrae, D. in *Handbook of Relativistic Quantum Chemistry* (ed Liu, W.) 51–81 (Springer Berlin Heidelberg, Berlin, Heidelberg, 2016). ISBN: 978-3-642-41611-8.

16. Lindgren, I. & Rosén, A. Relativistic self-consistent-field calculations with application to atomic hyperfine interaction. Part I: Relativistic self-consistent theory. *Case Studies in Atomic Physics* **4,** 97–149 (3 1974).

17. Froese Fischer, C., Brage, T. & Jönsson, P. *Computational Atomic Structure - An MCHF Approach* (Institute of Physics Publishing, 2000).

18. Jönsson, P. *et al.* An Introduction to Relativistic Theory as Implemented in GRASP. *Atoms* **11.** ISSN: 2218-2004. https://www.mdpi.com/2218-2004/11/1/7 (2023).

19. Slater, J. C. Atomic Shielding Constants. *Phys. Rev.* **36,** 57–64. https://link.aps.org/doi/10.1103/PhysRev.36.57 (1 July 1930).

20. Breit, G. Theory of Isotope Shift. *Rev. Mod. Phys.* **30,** 507–516. https://link.aps.org/doi/10.1103/RevModPhys.30.507 (2 Apr. 1958).

21. Bieroń, J., Froese Fischer, C., Gaigalas, G., Grant, I. & Jönsson, P. A Practical Guide to GRASP2018—A Collection of Fortran 95 Programs with Parallel Computing Using MPI. *The Computational Atomic Structure group* (2018).

22. Lindgren, I. & Morrison, J. *Atomic Many-Body Theory* 2nd ed. (Springer-Verlag, 1986).

23. Edmonds, A. R. *Angular Momentum in Quantum Mechanics* 2nd ed. Reptrinted as part of the Princeton Landmarks in Mathematics and Physics series in 1996. (Princeton University Press, 1960).

24. Jönsson, P., Parpia, F. & Fischer, C. HFS92: A program for relativistic atomic hyperfine structure calculations. *Computer Physics Communications* **96,** 301–310. ISSN: 0010-4655. https://www.sciencedirect.com/science/article/pii/0010465596000574 (1996).

25. Wilman, S., Elantkowska, M. & Ruczkowski, J. Fine- and hyperfine structure semi-empirical studies of the neutral and singly ionised bismuth. Determination of the nuclear quadrupole moment of 209Bi. *Journal of Quantitative Spectroscopy and Radiative Transfer* **275,** 107892. ISSN: 0022-4073. https://www.sciencedirect.com/science/article/pii/S0022407321003848 (2021).

26. Hull, R. J. & Brink, G. O. Hyperfine Structure of Bi^{209}. *Phys. Rev. A* **1,** 685–693. https://link.aps.org/doi/10.1103/PhysRevA.1.685 (3 Mar. 1970).

27. Rosenthal, J. E. & Breit, G. The Isotope Shift in Hyperfine Structure. *Phys. Rev.* **41,** 459–470. https://link.aps.org/doi/10.1103/PhysRev.41.459 (4 Aug. 1932).

28. Crawford, M. F. & Schawlow, A. L. Electron-Nuclear Potential Fields from Hyperfine Structure. *Phys. Rev.* **76,** 1310–1317. https://link.aps.org/doi/10.1103/PhysRev.76.1310 (9 Nov. 1949).

29. Bohr, A. & Weisskopf, V. F. The Influence of Nuclear Structure on the Hyperfine Structure of Heavy Elements. *Phys. Rev.* **77,** 94–98. https://link.aps.org/doi/10.1103/PhysRev.77.94 (1 Jan. 1950).

30. Persson, J. Table of hyperfine anomaly in atomic systems - 2023. *Atomic Data and Nuclear Data Tables* **154,** 101589. ISSN: 0092-640X. https://www.sciencedirect.com/science/article/pii/S0092640X23000177 (2023).

31. Bieroń, J. & Pyykkö, P. Nuclear Quadrupole Moments of Bismuth. *Phys. Rev. Lett.* **87,** 133003. https://link.aps.org/doi/10.1103/PhysRevLett.87.133003 (13 Sept. 2001).

32. Själander, M., Jahre, M., Tufte, G. & Reissmann, N. *EPIC: An Energy-Efficient, High-Performance GPGPU Computing Research Infrastructure* 2019. arXiv: 1912.05848 [cs.DC].

33. Gabriel, E. *et al.* Open MPI: Goals, Concept, and Design of a Next Generation MPI Implementation (eds Kranzlmüller, D., Kacsuk, P. & Dongarra, J.) 97–104 (2004).

34. Jönsson, P., Gaigalas, G., Bieroń, J., Fischer, C. F. & Grant, I. New version: Grasp2K relativistic atomic structure package. *Computer Physics Communications* **184,** 2197–2203. ISSN: 0010-4655. https://www.sciencedirect.com/science/article/pii/S0010465513000738 (2013).

35. Heggset, T. & Persson, J. R. Calculation of the Differential Breit-Rosenthal Effect in the 6s6p 3P1,2 States of Hg. *Atoms* **8.** ISSN: 2218-2004. https://www.mdpi.com/2218-2004/8/4/86 (2020).

36. Karlsen, M. K. & Persson, J. R. Calculation of the Differential Breit-Rosenthal Effect in Pb. *Atoms* **12.** ISSN: 2218-2004. https://www.mdpi.com/2218-2004/12/1/5 (2024).

37. Billowes, J. & Campbell, P. Laser spectroscopy of the bismuth isotopes. *Hyperfine Interactions* **129,** 289–301 (2000).

38. Schmidt, S. *et al.* The nuclear magnetic moment of 208Bi and its relevance for a test of bound-state strong-field QED. *Physics Letters B* **779,** 324–330. ISSN: 0370-2693. https://www.sciencedirect.com/science/article/pii/S0370269318301266 (2018).

39. Chuckrow, R. & Stroke, H. H. Hyperfine Structure and Isotope Shift of 30-Year 207Bi in the 3067-Å Resonance Line∗. *J. Opt. Soc. Am.* **61,** 218–222. https://opg.optica.org/abstract.cfm?URI=josa-61-2-218 (Feb. 1971).

40. Mariño, C. A. *et al.* Nuclear Magnetic Moments of ^{205,207,209}Bi Isotopes—Hyperfine Structure of the 15-day ^{205}Bi 3067-Å Line. *Phys. Rev. Lett.* **34,** 625–628. https://link.aps.org/doi/10.1103/PhysRevLett.34.625 (10 Mar. 1975).

41. Campbell, P. *et al.* Isotope shifts of the neutron-deficient bismuth isotopes: charge radii systematics across the Z = 82 shell closure. *Physics Letters B* **346,** 21–26. ISSN: 0370-2693. https://www.sciencedirect.com/science/article/pii/037026939500014C (1995).

Appendix A

Script examples

In the tables below, the scripts for a calculation of 6sp5spd4spdf→4spdfg1h using method VI will be given, to illustrate the computational workflow of the present work. The leftmost column will give the line number, the middle column contains the inputs used in this calculation, and the rightmost column contains slightly rewritten versions of the prompts each input corresponds to.

#	Filename: init	Corresponding prompt in GRASP
	SLURM PREAMBLE	
1	rcsfgenerate <<EOF1	
2	u	Default, reverse, symmetry or user specific ordering?
3	3	Select core
4	3d(10,c)4s(2,*)4p(6,*)4d(10,*)4f(14,*)5s(2,*)5p(6,*)5d(10,*)6s(2,*)6p(3,*)	Give configuration 1
5		Give configuration 2
6	10s,10p,9d,8f,8g,6h	Give set of active orbitals
7	1,5	Resulting 2*J-number?
8	1	Number of excitations
9	y	Generate more lists?
10	3d(10,c)4s(2,i)4p(6,i)4d(10,i)4f(14,i)5s(2,i)5p(6,i)5d(10,i)6s(2,*)6p(3,*)	Give configuration 1
11		Give configuration 2
12	10s,10p,9d,8f,8g,6h	Give set of active orbitals
13	1,5	Resulting 2*J-number?
14	2	Number of excitations
15	y	Generate more lists?
16	3d(10,c)4s(2,i)4p(6,i)4d(10,i)4f(14,i)5s(2,1)5p(6,i)5d(10,i)6s(2,*)6p(3,*)	Give configuration 1
17	3d(10,c)4s(2,i)4p(6,i)4d(10,i)4f(14,i)5s(2,i)5p(6,5)5d(10,i)6s(2,*)6p(3,*)	Give configuration 2
18	3d(10,c)4s(2,i)4p(6,i)4d(10,i)4f(14,i)5s(2,i)5p(6,i)5d(10,9)6s(2,*)6p(3,*)	Give configuration 3
19		Give configuration 4
20	7s,7p,6d,5f,5g,6h	Give set of active orbitals
21	1,5	Resulting 2*J-number?
22	2	Number of excitations
23	n	Generate more lists?
24	EOF1	
25		

	Filename: init	
26	\cp rcsf.out rcsf.inp	
27		
28	rcsfinteract <<EOF2	
29	2	DC Hamiltonian (1) or DCB Hamiltonian (2)?
30	EOF2	
31		
32	\cp rcsf.out rcsf.inp	
33		
34	rwfnestimate <<EOF3	
35	n	Default settings?
36	n	Generate debug printout?
37		File erwf.sum will be created...
38	y	Change default speed of light or grid parameters?
39	n	Change speed of light?
40	y	Change grid parameters?
41	1.2048192771084337E-008	Enter RNT:
42	1E-002	Enter H:
43	0	Enter HP:
44	2990	Enter N:
45	1	Read subshell radial wave function
46	rwfn_20V3	Enter the filename:
47	*	List of relativistic subshells:
48	2	*In case some subshells cannot be estimated by (1)*
49	*	List of relativistic subshells:
50	3	*In case some subshells cannot be estimated by (2)*
51	*	List of relativistic subshells:
52	n	Revise estimates?
53	EOF3	
54		
55	sbatch rang	*Initiate rangular*

#	Filename: rangular	Corresponding prompt in GRASP
	SLURM PREAMBLE	
1	mpirun rangular_mpi <<EOF4	
2	y	Full interaction?
3	EOF4	
4		
5	sbatch rmcdhf	*Initiate rmcdhf*
	Filename: rmcdhf	
	SLURM PREAMBLE	
1	mpirun rmcdhf_mpi <<EOF5	
2	n	Default settings?
3	n	Generate debug output?
4	y	Change default speed of light or grid parameters?
5	n	Change speed of light?
6	y	Change grid parameters?
7	1.2048192771084337E-008	Enter RNT:
8	1E-002	Enter H:
9	0	Enter HP:
10	2990	Enter N:
11	n	Change default accuracy?
12	1	Enter ASF serial numbers for block 1
13	1-3	Enter ASF serial numbers for block 2
14	1	Enter ASF serial numbers for block 3
15	5	Level weights
16	11s,11p-,11p,10d-,10d,9f-,9f,9g-,9g,6h-,6h	Enter orbitals to be varied
17		Which of these are spectroscopic?
18	50	Maximum number of iterations
19	n	Modify other defaults?
20	1	Orthonormalization order?
21	EOF5	
22		
23	\ cp rwfn.out rwfn_20V4	
24	rsave 20V4	
25		
26	sbatch rci	*Initiate rci*

#	Filename: rci	Corresponding prompt in GRASP
	SLURM PREAMBLE	
1	mpirun rci_mpi <<EOF6	
2	y	Default settings?
3	20V4	Name of state?
4	y	Include transverse-photon interaction?
5	y	Modify all transverse photon frequencies?
6	1.d-6	Enter scale factor
7	y	Include vacuum polarization?
8	n	Include normal mass shift?
9	n	Include specific mass shift?
10	y	Estimate self-energy?
11	7	Largest principal quantum number for self-energy?
12	1	Enter ASF serial numbers for block 1
13	1-3	Enter ASF serial numbers for block 2
14	1	Enter ASF serial numbers for block 3
15	EOF6	
16		
17	sbatch rhfs	*Initiate rhfs*

#	Filename: rhfs	Corresponding prompt in GRASP
	SLURM PREAMBLE	
1	rhfs <<EOF7	
2	n	Default settings?
3	20V4	Name of state
4	y	Mixing coefficients from a CI calculation?
5	n	Generate debug printout?
6	n	Change speed of light?
7	n	Treat some contributions as first-order perturbations?
8	y	Change grid parameters?
9	1.2048192771084337E-008	Enter RNT:
10	1E-002	Enter H:
11	0	Enter HP:
12	2990	Enter N:
13	EOF4	

Appendix B

Figure 9.10, extended

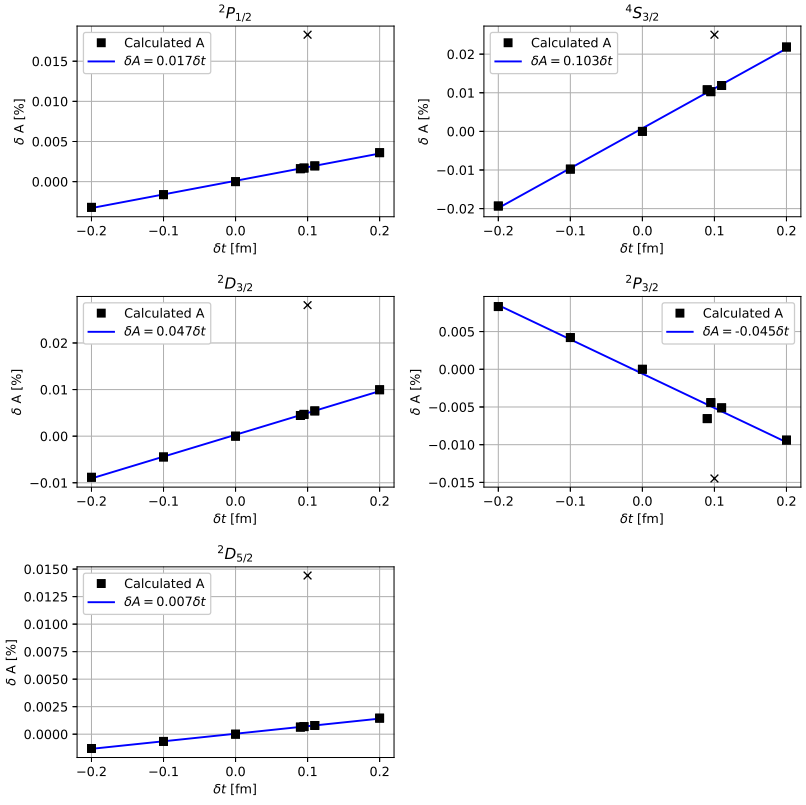

Figure B.1: Linear fit of the relation $\delta A = \tau \delta t$ for method VIII, with erroneous values indicated as "x". Note that these values were not included in the linear fit.

Appendix C

Full tables of expansion sizes

Included here are the number of CSFs for all steps in all methods. These tables are intended as supplementary material to the figures in chapter 9 (9.1-9.8), meant to serve as a guide to the expected accuracies available at different expansion sizes.

C.1 Methods I-IV

Table C.1: Expansion sizes for all calculations done with methods I-IV

Mthd.	From	Exc.	To	NCF	Mthd.	From	Exc.	To	NCF
I	6sp	S	1spdf	107	II	6sp	SD	1spdfgh	1 341
			2psdf	209				2spdfg1h	4 536
			3spdf	311				3spdfg1h	9 629
			4spdf	413				4spdfg1h	16 620
	6sp5spd	S	1spdf	637		6sp5spd	SD	1spdfgh	61 501
			2spdf	1 250				2spdfg1h	208 668
			3spdf	1 863				3spdfg1h	444 499
			4spdf	2 476				4spdfg1h	768 994
	6sp5spd4spdf	S	1spdf	1 469	III	6sp	SDT	1spdfgh	20 981
			2spdf	2 880				2spdf1gh	116 822
			3spdf	4 291				3spdf1gh	347 131
			4spdf	5 702				4spdf1gh	771 194
	6sp5spd4spdf3sp	S	1spdf	1 774					
			2spdf	3 471					
			3spdf	5 168					
			4spdf	6 865					
Mthd.	From	Exc.	To	NCF					
IV	6sp	SrD	1spdfgh	1 341					
			2psdfg1h	4 536					
			3spdfg1h	9 629					
			4spdfg1h	16 620					
	6sp5spd	SrD	1spdfgh	19 499					
			2spdfg1h	66 724					
			3spdfg1h	142 603					
			4spdfg1h	247 136					
	6sp5spd4spdf	SrD	1spdfgh	51 513					
			2spdfg1h	173 492					
			3spdfg1h	368 359					
			4spdfg1h	636 114					
	6sp5spd4spdf3p	SrD	1spdfgh	57 884					
			2spdfg1h	194 848					
			3spdfg1h	413 732					
			4spdfg1h	714 496					

C.2 Methods V and VI

Table C.2: Expansion sizes for all calculations done with methods V and VI

Mthd.	From	Exc.	To	NCF	Mthd.	From	Exc.	To	NCF
V	6sp	SD	1spdfgh	1 341	VI	6sp	SD	1spdfgh	1 341
			2psdfg1h	4 536				2psdfg1h	4 536
			3spdfg1h	9 629				3spdfg1h	9 629
			4spdfg1h	16 620				4spdfg1h	16 620
	6sp5spd	SD	1spdfgh	61 501		6sp5spd[1]	SD	1spdfgh	61 501
	6sp5spd	S	2spdfg1h	65 329		6sp5spd	S	2spdfg1h	23 327
	6sp	SD	2spdfg1h			6sp	SD	2spdfg1h	
	6sp5spd	SD	1spdfgh			6sp5spd	SrD	1spdfgh	
	6sp5spd	S	3spdfg1h	71 055		6sp5spd	S	3spdfg1h	29 053
	6sp	SD	3spdfg1h			6sp	SD	3spdfg1h	
	6sp5spd	SD	1spdfgh			6sp5spd	SrD	1spdfgh	
	6sp5spd	S	4spdfg1h	78 679		6sp5spd	S	4spdfg1h	36 677
	6sp	SD	4spdfg1h			6sp	SD	4spdfg1h	
	6sp5spd	SD	1spdfgh			6sp5spd	SrD	1spdfgh	
	6sp5spd4spdf	S	1spdfgh	62 578		6sp5spd4spdf	S	1spdfgh	20 576
	6sp5spd	SD	1spdfgh			6sp5spd	SrD	1spdfgh	
	6sp5spd4spdf	S	2spdfg1h	67 326		6sp5spd4spdf	S	2spdfg1h	25 324
	6sp	SD	2spdfg1h			6sp	SD	2spdfg1h	
	6sp5spd	SD	1spdfgh			6sp5spd	SrD	1spdfgh	
	6sp5spd4spdf	S	3spdfg1h	73 972		6sp5spd4spdf	S	3spdfg1h	31 970
	6sp	SD	3spdfg1h			6sp	SD	3spdfg1h	
	6sp5spd	SD	1spdfgh			6sp5spd	SrD	1spdfgh	
	6sp5spd4spdf	S	4spdfg1h	82 516		6sp5spd4spdf	S	4spdfg1h	40 514
	6sp	SD	4spdfg1h			6sp	SD	4spdfg1h	
	6sp5spd	SD	1spdfgh			6sp5spd	SrD	1spdfgh	
	6sp5spd4spdf3sp	S	1spdfgh	62 902		6sp5spd4spdf3sp	S	1spdfgh	20 900
	6sp5spd	SD	1spdfgh			6sp5spd	SrD	1spdfgh	
	6sp5spd4spdf3sp	S	2spdfg1h	67 945		6sp5spd4spdf3sp	S	2spdfg1h	25 943
	6sp	SD	2spdfg1h			6sp	SD	2spdfg1h	
	6sp5spd	SD	1spdfgh			6sp5spd	SrD	1spdfgh	
	6sp5spd4spdf3sp	S	3spdfg1h	74 886		6sp5spd4spdf3sp	S	3spdfg1h	32 884
	6sp	SD	3spdfg1h			6sp	SD	3spdfg1h	
	6sp5spd	SD	1spdfgh			6sp5spd	SrD	1spdfgh	
	6sp5spd4spdf3sp	S	4spdfg1h	83 725		6sp5spd4spdf3sp	S	4spdfg1h	41 723
	6sp	SD	4spdfg1h			6sp	SD	4spdfg1h	
	6sp5spd	SD	1spdfgh			6sp5spd	SrD	1spdfgh	

C.3 Methods VII and VIII

Table C.3: Expansion sizes for all calculations done with methods VII and VIII. Since these were modifications of method VI, they were only done with the maximal spectroscopic sets. The highlighted rows of method VII were those for which only configurations resulting in J=3/2 were allowed.

Mthd.	From	Exc.	To	NCF
VII	6sp5spd4spdf3sp	S	1spdfgh	38 296
	6sp	SD	1spdfgh	
	6sp5spd4spd[2]	SrD	1spdfgh	
	6sp5spd4spdf3sp	S	2spdfg1h	66 085
	6sp	SD	2spdfg1h	
	6sp5spd	SrD	1spdfgh	
	6sp5spd4spd	**SrD**	**2spdfg1h**	
	6sp5spd4spdf3sp	S	3spdfg1h	123 989
	6sp	SD	3spdfg1h	
	6sp5spd	SrD	1spdfgh	
	6sp5spd4spd	**SrD**	**3spdfg1h**	
	6sp5spd4spdf3sp	S	4spdfg1h	203 299
	6sp	SD	4spdfg1h	
	6sp5spd	SrD	1spdfgh	
	6sp5spd4spd	**SrD**	**4spdfg1h**	
VIII	6sp5sp4sp3sp2sp1s	S	1spdfgh	10 339
	6sp5sp	SrD	1spdfgh	
	6sp5sp4sp3sp2sp1s	S	2spdfg1h	14 791
	6sp	SD	2spdfg1h	
	6sp5sp	SrD	1spdfgh	
	6sp5sp4sp3sp2sp1s	S	3spdfg1h	21 141
	6sp	SD	3spdfg1h	
	6sp5sp	SrD	1spdfgh	
	6sp5sp4sp3sp2sp1s	S	4spdfg1h	29 389
	6sp	SD	4spdfg1h	
	6sp5sp	SrD	1spdfgh	

[1]This was accidentally run with unrestricted SD excitations.
[2]This was accidentally run without the J=3/2 restriction.

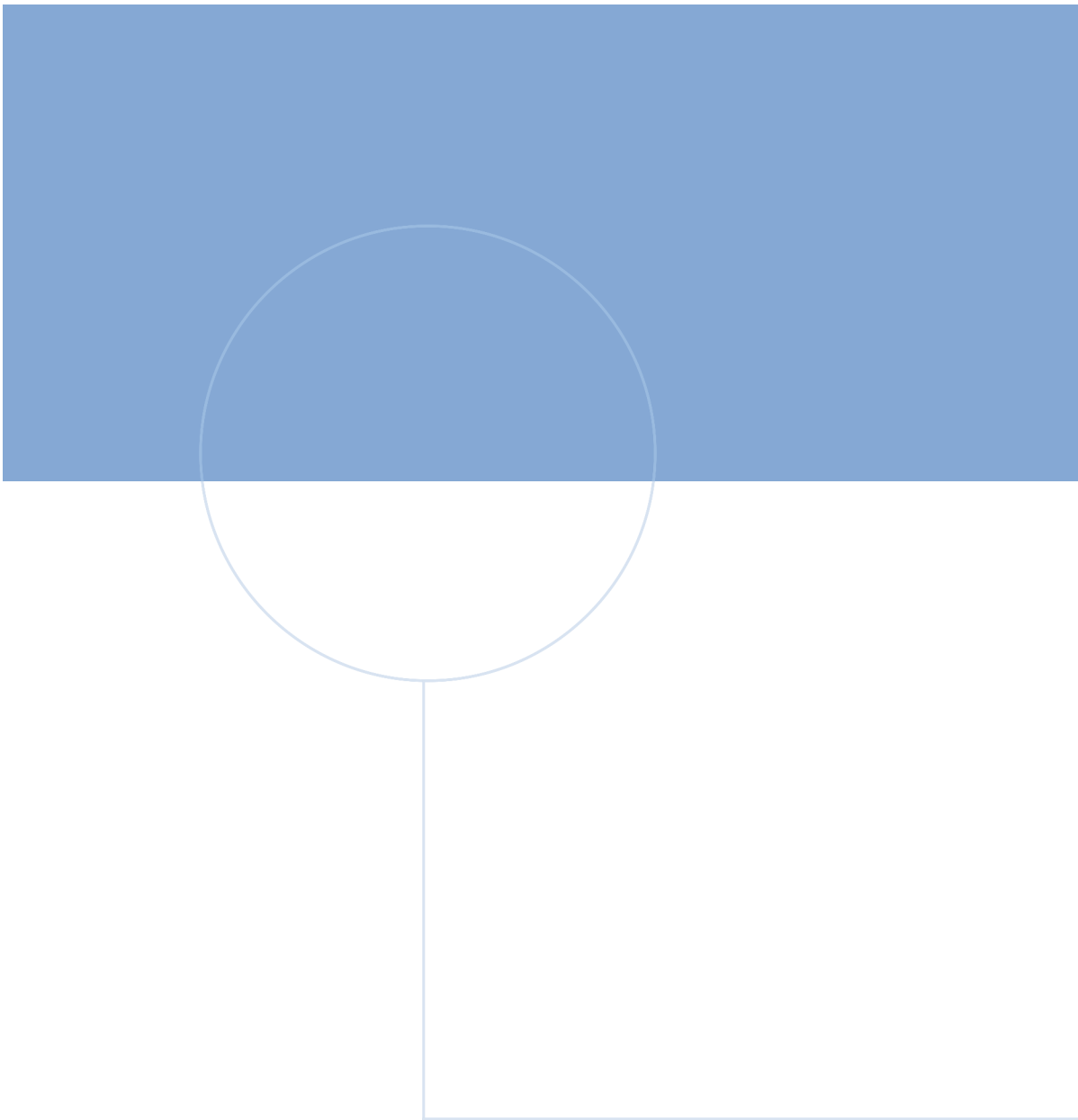

NTNU

Norwegian University of
Science and Technology